ADDIS ABABA UNIVERSITY

ADDIS ABABA INSTITUTE OF TECHNOLOGY

SCHOOL OF MULTI-DISCIPLINARY ENGINEERING

CENTER FOR MATERIALS ENGINEERING

PHOTOCATALYTIC DEGRADATION OF METHYLENE BLUE USING IRON DOPED TiO_2 POROUS SHELL UNDER LIGHT IRRADIATION

Thesis Submitted to Center for Materials Engineering, Addis Ababa Institute of Technology, in Partial Fulfilment of the Requirements for the Degree of Masters in Materials Engineering.

By

Mariamsina Kassahun Bekele (M.Sc.)

September 2021

Addis Ababa, Ethiopia

ADDIS ABABA UNIVERSITY

ADDIS ABABA INSTITUTE OF TECHNOLOGY

CENTER FOR MATERIALS ENGINEERING

This is to certify that the thesis prepared by **Mariamsina Kassahun** entitled “**Photocatalytic Degradation of Methylene blue using Fe doped TiO_2 Porous shell under Light Irradiation**.” and submitted in partial fulfillment of the requirements for the Degree of Master of Science in Materials Engineering complies with the regulations of the university and meets the accepted standards concerning originality and quality.

Approved by Board of Examiners

Tesfaye Refera (Ph.D.) Advisor	Signature	Date
Girum Ayalneh (Ph.D) Co-Advisor	Signature	Date
Georgies Alene(Ph.D) Internal Examiner	Signature	Date
Shimeles Kebede(Ph.D) External Examiner	Signature	Date
Anteneh Mareilgn(Ph.D) Chair man	Signature	Date

DECLARATION

Hereby, I declare that this M.Sc. thesis is my original work and not submitted in any previous application for a degree in any other university. In addition, the source of materials used for this thesis has been appropriately acknowledged.

Mariamsina Kassahun Bekele		
Name of Student	Signature	Date

ABSTRACT

Titanium dioxide is a well-known photocatalyst for the photodegradation of dyes like methylene blue. However, its application is limited due to its wide bandgap and higher recombination rate of photogenerated electrons and holes. This work shows that doping transition metals lead to reducing the bandgap and increasing surface area to improve the degradation efficiency of titanium dioxide (TiO_2). Iron doped TiO_2 hollow and porous spheres with different Fe-doping contents were prepared based on a sol-gel synthesis. Melamine formaldehyde (MF) has been used as a sacrificial template, and cetyltrimethylammonium bromide (CTAB) was used as a pore-directing agent. By calcining the composite spheres at 450, 500, 550 ◦C for three h in air, and in situ Fe doped TiO_2 hollow and porous spheres process occurred upon the decomposition of the MF template and CTAB pore-directing surfactant. The 0.25wt% Fe-doped porous TiO_2 hollow nanosphere at 450^{o}C exhibited a significantly narrower optical bandgap and higher photocatalytic activity in the removal of Methylene blue (MB) than that of the pure THPNS. The composition and Fe-doping content, thermal stability, morphology, surface area, and pore size distribution, photocatalytic activities, and optical properties of the porous TiO_2 hollow spheres derived from different conditions were investigated and compared based on X-ray diffraction (XRD), Fourier-transformation infrared ray spectroscopy (FT-IR), Scanning electron microscope (SEM), Brunauer-Emmett-Teller (BET) Thermogravimetric analysis (TGA/DTA), Diffuse reflection spectroscopy (DRS analysis), Zeta sizer, and Ultraviolet-Visible (Uv-Vis) Spectroscopy techniques. The effect of dye concentration, dopant concentration, pH of the dye solution, catalyst loading, and calcination temperature on the characteristics, photocatalytic activities, and optical properties of the hollow and porous TiO_2 Nanosphere has been studied and discussed.

Keywords-Titanium dioxide, Fe dopant, Hollow and Porous sphere morphology, Photocatalyst.

ACKNOWLEDGMENT

First and foremost, I praise and thank Almighty God for His showers of blessings throughout my life and my research work to complete the research successfully.

I would like to express my sincere gratitude to my advisor Dr. Tesfaye Refera, and co-Advisor Dr. Girum Ayalneh, for their continued support, patience, motivation, enthusiasm, and immense knowledge. Their guidance helped me in all the research and writing of this thesis. I could not have imagined having a better advisor and mentor for my Thesis work.

Besides my advisors, I would like to thank Dr. Sintayehu Nibret for his valuable and constructive suggestions during the planning and working on the thesis.

My deep gratitude goes to my families and friends for their support and encouragement. In addition, my special thanks go to Mr. Demeke Tesfaye and Mr. Henok Girma, for their patience, inspiring support, and facilitation, throughout all of the laboratory activities of this research work.

Lastly, I would like to thank the Materials Engineering Department and Addis Ababa Science and Technology University for providing this Masters female scholarship.

LIST OF TABLES

LIST OF FIGURES

LIST OF ACRONYMS

BET	Brunauer-Emmett-Teller
CTAB	Cetyltrimethyl ammonium bromide
DRS	Diffuse Reflection spectroscopy
DTA	Differential thermal analysis
FT-IR	Fourier-transformation infrared ray spectroscopy
HK	Horvath-Kawazoe Method
MB	Methylene blue
MF	Melamine-Formaldehyde
SEM	Scanning electron microscopy
SF	Saito-Foley Method
TGA	Thermogravimetric analysis
THPNS	Titanium hollow and porous Nanosphere
Uv-Vis	Ultraviolet-visible
XRD	X-ray diffraction

TABLE OF CONTENTS

REFERENCE

APPENDIX

CHAPTER ONE

1. INTRODUCTION

1.1 Background

The global spread of various contaminants released from factories that primarily use dyes has become the most crucial concern. In addition, the dye's complex and stable structure makes degradation more difficult (Scholz 2018). Since contaminants such as heavy metals, inorganic compounds, organic pollutants, and other compounds persist in wastewater, unregulated disposal leads to an undesirable effect on human lives and the climate. As a consequence, the wastewater should be treated before it is discharged into the atmosphere.

Nanotechnology plays a significant role in manufacturing technologies, electronics, telecommunications, health, and environmental remediation. This technology involves producing and utilizing a diverse array of nanomaterials with a size ranging from 1 to 100 nm and display unique properties not found in bulk-sized materials (Xu et al., 2012). Mainly, three-dimensional (3D) nanostructures with complex morphology and high dimensionality have gained great research interest. Their advanced geometric structure and atom arrangement on the specific facets of these nanostructures can offer novel properties (Huang et al., 2015).

There is an urgent need to explore environmentally friendly technologies applicable to pollutant removal or recovery to attain sustainable development in a clean environment. One of the current research areas in this regard is photocatalysis, which is a part of the Advanced Oxidation process that has been proven to be a promising green technology for organic synthesis, water splitting, photoreduction, hydrogen transfer, isotopic exchange, metal deposition, water purification and gaseous pollutant detoxification (Lum et al. 2020).

Advanced oxidation processes are used to oxide complex organic contaminants found in wastewater and that are difficult to degrade into end products through biological processes. For a photocatalyst to be perceived as good, it should be biologically and chemically inert, photoactive, able to utilize visible or near Uv light, inexpensive, photostable, and non-toxic. Some examples of catalysts include Si, ZnO, WO_3, TiO_2, CdS, $SrTiO_3$, ZnS, SnO_2, Fe_2O_3 WSe_2.

The most commonly used catalyst is Titanium dioxide (TiO_2); it has been demonstrated as an excellent catalyst for the photo-oxidation of various inorganic and organic compounds.

Reports show that TiO_2 exists in three polymorphs such as rutile, anatase, and brookite. Among these, the anatase phase has been proven to be the most efficient photocatalytic activity, high stability. However, its large bandgap limits its absorption of solar radiation, rapid recombination of photogenerated electron-hole pairs will reduce photocatalytic efficiency. Therefore, several modification techniques have been applied to overcome the drawbacks, which leads to enhance the photocatalytic activities of TiO_2. These are: metal and non-metal doping, dye sensitization, surface modification, fabrication of heterostructure, immobilization, and stabilization on support structure are some of the approaches reported.

In this study, photodegradation efficiency of Iron doped TiO_2 hollow and porous nanosphere made with melamine-formaldehyde (MF) sphere as a sacrificial template and Cetyl trimethyl ammonium bromide (CTAB) as a pore directing agent under visible light irradiation towards the removal of Methylene blue (MB) dye have been investigated.

1.2 Statement of the problem

Dyes can remain in the environment for an extended period because of their high thermal and photostability properties to resist biodegradation. The significant environmental concern with dyes is their absorption and reflection of sunlight entering the water. Light absorption diminishes the photosynthetic activity of algae and influences the food chain. Photocatalysts were used to degrade the effluents before it released from the industries to overcome the effects. There are also known drawbacks regarding TiO_2 photocatalyst related to the bandgap, surface area, morphology, crystallinity, adsorption of light, particle size.

1.3 Objective

1.3.1 General Objective

The general objective of the study is to enhance the photocatalytic activity of TiO_2 through the doping and surface adjustment method. The study aims to photocatalytic removal of methylene blue utilizing Fe- doped hollow TiO_2 Nanosphere with porous shell under visible light irradiation.

1.3.2 Specific Objective

- To synthesize soft templates for synthesis of TiO_2 using melamine and formaldehyde.
- To synthesize and characterize hollow and porous TiO_2 nanospheres.
- To investigate the influence of different iron concentrations on the photocatalytic activity of hollow and porous TiO_2 nanosphere.
- To study the conditions for photocatalytic removal of methylene blue (pH, catalyst loading, dye concentration, calcination temperature of the photocatalyst, and irradiation time).
- To evaluate the Photocatalytic performance of the sample in the removal of Methylene blue.

1.4 Significance of the research

The significance of this study is to address how to enhance the photocatalytic activity of TiO_2 by using various modification techniques and controlled parameters to remove and decolorize Methylene blue. By doping iron on TiO_2 leads to form trapping state to reduce the band gap. The other modification technique used in this paper is forming hollow and porous TiO_2 shell to enhance the surface area.

1.5 Scope of the research

In this study, the adjustment techniques towards reducing the bandgap and enhancing the surface area is used to trap more lights and improving the number of photogenerated electrons and holes. Fe doped TiO_2 hollow sphere with porous walls that satisfy a situation of high crystallinity, controllable morphology and size, low density, high surface area achieved through sol-gel synthesis and the template removed through calcination process. Removal of methylene blue investigated and studied through the influence of calcination temperature, pH of methylene blue solution, catalyst loading, dye concentration and reusability of the catalyst.

CHAPTER TWO

2. LITERATURE REVIEW

2.1 Photocatalytic Nanomaterials

In the past few years, micro/nano architectures of highly ordered have attracted considerable interest in materials due to their unique properties and potential applications in many fields. Significantly, three dimensional (3D) nanostructures with complex morphology and high dimensionality have received great research interest since their advanced geometric structure, and atom arrangement on the specific facets of these nanostructures can offer novel properties, which caused their potential applications in various fields, such as electronics, catalysis, gas-sensing, optics, photodegradation, and water treatment. Up to date, several methods such as template-assisted growth, thermolysis, and hydrothermal or solvothermal processes were reported to synthesize 3D hierarchical structures (Huang et al., 2015).

An excessive deal of attention has recently been paid to the development of photocatalyst, which is being used in various products and research areas, especially for environmental and energy applications. Semiconductor-based photocatalysts have been extensively studied due to their electronic configuration to absorb applied solar spectrum for photocatalytic reaction. The semiconductor consists of a valence band (VB) and conduction band (CB). The energy difference between the top of the VB and the bottom of the CB levels is known as bandgap energy (Eg) which is responsible for photoactivity of the semiconductor (Bashiri and Mohamed 2017). The general principle of photocatalytic reaction over the semiconductor is summarized in the following steps; 1). Harvesting photons with energy equivalent or higher than the bandgap energy to form electron-hole pairs. 2). Photogenerated electrons are injected into the CB, while photogenerated holes with a positive charge are left behind in the VB. 3). Surface chemical reactions consist of reducing an acceptor species and oxidizing a donor species (Bashiri and Mohamed 2017). Semiconducting oxides such as TiO_2, $SrTiO_3$, ZnO, α-Fe_2O_3, WO_3, Ta_2O_5, VO_2, $KTaO_3$, and Fe_2O_3 appear to be the most considered materials for photocatalysts because their properties can be modified over wide ranges through changing their semiconducting properties. Moreover, these materials are economically promising because their processing technologies are relatively simple. TiO2 is one of the most significant photocatalysts used for numerous energy and environmental applications among different metal oxides.

2.2 Titanium dioxide photocatalyst

Titanium dioxide (TiO_2) is one of the essential functional transition metal oxides due to its superior physical and chemical properties such as long-term stability against chemical corrosion and photo corrosion, strong oxidizing ability,and facile preparation; which makes it widely used in photocatalysis (Wan et al. 2018), high-performance hydrogen production (Singh and Dutta 2018), sensors (Seif, Nikfarjam, and Haj 2019), electrochemical, dye-sensitized solar cell (Zhao et al. 2016), lithium-ion battery (Cao et al. 2018), solar cell, detoxification and so on. Pure TiO_2 is commonly photoactivated by Uv light owing to its wide bandgap (3.2 eV for anatase and 3.0 eV for rutile phase TiO_2) (Kumaravel et al. 2019). Surface decoration or inclusion of appropriate materials in TiO_2 can favor its visible-light absorption for practical applications. Among the three crystalline phases of TiO_2 (anatase, rutile, and brookite), the anatase phase shows maximum photocatalytic activity. The lifetime of photogenerated charge carriers in the anatase phase is longer than that of the rutile and brookite phases. However, its large bandgap limits its absorption of solar radiation, rapid recombination of photogenerated electron-hole pairs, poor affinity towards organic pollutants will reduce photocatalytic efficiency. Several modification techniques have been applied to enhance the photocatalytic activities of TiO_2. These are: metal and non-metal doping, dye sensitization, surface modification, fabrication of heterostructure, immobilization, and stabilization on support structure are some of the approaches reported. In recent years, the improvement of TiO_2 surface applied to increase surface area; that leads to trapping more light for making a significant amount of Photogenerated electrons and holes. Substantial effort has been devoted to fabricating various TiO_2 nanostructures and morphologies, including TiO_2 nanospheres (Ding et al. 2019), nanorods (Jia et al. 2019), nanotubes (Huang et al. 2015), nanosheets (Zhang et al. 2017), nanoholes (Zada et al. 2017), nanofibers (Zhang and Yu 2019), thin-film (AL-Jawad, Taha, and Salim 2017) and other hierarchical nanostructures. Among them, 3D TiO_2 nanostructures have been considered a promising candidate due to their high surface area, low density, high light-harvesting efficiency, and good surface permeability. Numerous 3D TiO_2 nanostructures have been synthesized in the past few years. The synthesis condition and methodology have strongly influenced the photocatalytic activity of TiO2. Various methods have been applied for the synthesis of TiO_2 photocatalyst: electrochemical, combining inverse micelle and plasma treatment (Yen et al. 2017), dip coating, microwave (Alosfur and Ridha 2018), two-step wet chemical, precipitation, hydrothermal (Ye et al. 2010), and solvothermal (Zhuang, Zhou, and Liu 2013), chemical solvent, and chemical vapor decomposition, ultrasonic irradiation (Zarnaghash et al. 2019), two-route sol-gel, and sol-gel (Kaygili et al. 2017), hydrolysis (Li and Zeng 2007).

2.3 Hollow and porous TiO_2 photocatalyst

2.3.1 Hollow and porous nanosphere

Hollow nanostructures with controlled chemical composition and morphology have arisen as an essential structure of materials. These nanostructures can be observed as particulate materials with interior cavities and uniform morphologies, exhibiting well-defined boundaries. Moreover, since the existence of holes, the surface area of the particles is considerably larger. However, the density is much lower than that of their dense solid counterparts for equal volumes of material. Indeed, hollow nanostructures are regarded as functional nanomaterials with attractive properties such as high specific surface areas, large pore volume, and high loading capacity, which endow them with potential applications.

2.3.2 Preparation methods of hollow and porous

Techniques to prepare hollow particles were categorized into three groups, namely sacrificed template methods, in-situ template methods, and device-based methods.

1. Sacrificed template method or hard templating strategy

This technique was described as the preparation of hollow particles by coating a template such as organic bead template (Sandoval et al. 2012), emulsion template, surfactant vesicle template, $CaCO_3$ template, SiO_2 template(Zhang, Li, and Yang 2014), and Hydroxyapatite (HAp) template with a thin layer of the precursor through a sol-gel process or layer-by-layer (LBL) self-assembly technique and subsequent organic cores are removed by calcination or thermal decomposition, chemical dissolution forming hollow particles. Hard-templating methods for the fabrication of hollow structures are generally simple, effective, and straightforward. Typically, the process involves four main steps: formation of the hard template material; naturally, an inorganic compound or polymer that can be chemically etched in a subsequent step, chemical modification of the template’s surface; coating the template by growing a distinct inorganic phase, and selective removal of the internal template to obtain the hollow structures. Adjusting the template's surface might involve chemical functionalization, which is generally challenging because it requires robust methods to efficiently precipitate the shell materials on substrates with sizes in the micro/nanometer range. On the other hand, the chemical functionalization of the hard template surface can improve the compatibility with the shells. Three main approaches have been used to remove the template such as chemical etching, thermal treatment, or dissolving the template in an appropriate solvent, which is very common in the case of a polymer template.

2. In-situ template method or soft templating method

In recent times, exciting results have been reported to fabricate hollow particles without using the supplementary template, called the in-situ template method. The in-situ template method contains the in-situ reactant template method and the in-situ product template method. For the in-situ reactant template method, hollow particles are designed by directly coating/precipitation nanocrystals on the surface of reactants that would be consumed in the following reactions. After the response, the templates are disbursed, and hollow particles are directly obtained without further treatment to remove the templates. For the in-situ product templates method, hollow particles form on the surface of the interim product, which has been removed after the reaction. These methods make it easier to refill the hollow interior with dispersed functional species or encapsulate in-situ guest molecules during shell formation. However, compared with other approaches, the control of particle shape can be more difficult using soft methods: Emulsion templating, Vesicle/micelle templating, gas bubble templating, and electrospray.

3. Device-based method or self templating method

Hollow materials have been prepared by taking advantage of self-templating methods that are not dependent on an external templating agent and thus require fewer steps for their preparation. This approach is followed to reduce the production cost and facilitate the large-scale synthesis of hollow materials. Some approaches can directly synthesize hollow structures, such as etching, Ostwald ripening, Kirkendall effect, and galvanic replacement. Overall, most of these methods hang on a two-step approach; the synthesis of the non-hollow material followed by the conversion of this material into hollow structures. The direct synthesis offers several advantages over the template-based ones, such as reproducibility and superior control over the shell thickness and particle size distribution (Shang, Jiao, and Chen 2012).

2.4 Polymer template

This method is designed to prepare hollow particles by using some organic beads such as poly-styrene (PS) spheres (Qiao, Chen, and Wu 2010), Polymethyl methacrylate (PMMA) (Islam et al. 2017), Melamine formaldehyde (MF) sphere is used as templates which are coated by desired materials. After coating, the organic cores are removed by calcination or decomposition to form hollow particles.

2.5 Melamine formaldehyde sphere

Melamine (1, 3, 5-tri amino-2, 4, 6-triazine) formaldehyde (MF) is one of the hardest and stiffest thermosetting polymers, which provides good properties and performance. It is an amino resin and has various material advantages, such as transparency, better hardness, thermal stability, excellent boil resistance, scratch resistance, abrasion resistance, flame retardant, moisture resistance, and surface smoothness, which lead MF to large industrial applications (Merline 2013) because of their monodisperse sizes, stable surface charge distribution, solubility in an appropriate solvent, and the volatile of calcined products (Liu et al. 2012).

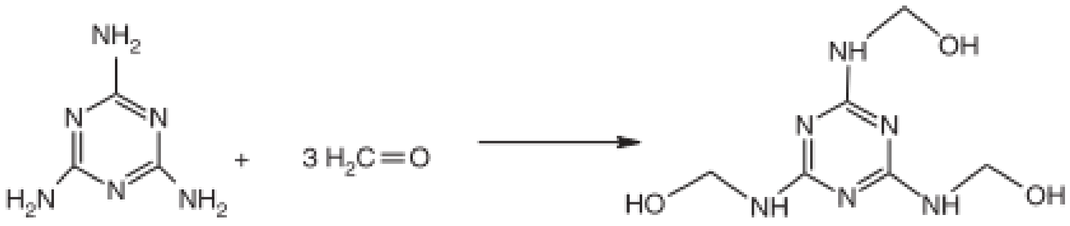

Melamine + Formaldehyde → Metylomelamin

Figure 2. 1 Chemical formation of Melamine formaldehyde.

Melamine–formaldehyde (MF) resin polymers are derived from the polycondensation of melamine and formaldehyde molecules. In addition to their advanced thermal and solvent stabilities, MF resin spheres have several advantages, such as a relatively high density of 1.51 g cm^{-3} (compared with 1.05 g cm^{-3} for PS and 1.19 g cm^{-3} for PMMA), a relatively high refractive index of 1.68 (compared with 1.59 for PS and 1.48 for PMMA) and a cationic surface. All these features make MF spheres chosen materials in various fields. For example, MF resin polymer colloidal spheres have been effectively used as template particles in fabricating hollow polyelectrolyte structures (Wu et al. 2013).

2.6 Different dopant effects on TiO_2 HPT sphere

Literature shows different techniques to enhance the photocatalytic performance of TiO_2, among them different metal and nonmetals doped on TiO_2 to reduce the bandgap while the other is to increase the surface area of TiO_2 to trap more light to generate photoelectron and hole. 3D structures using different hard templates such as PS, PMMA, Carbon, SiO_2, and MF spheres were successfully investigated through many processes. For instance, yttrium-doped TiO_2 hollow spheres (Y-TiO_2HS) were successfully prepared via a sol-gel method using melamine-formaldehyde polymer microspheres as a template, (Jiang et al. 2017). Three kinds of N-doped mesoporous TiO_2 hollow spheres with different N-doping contents, surface area, and pore size distributions were prepared based on a sol–gel synthesis and combined with a calcination process (Li 2016). Titanium hollow spheres were fabricated successfully using tetra butyl titanate as titanium precursor and colloidal carbon spheres as a hard template (Liu et al. 2015). A simple hydrothermal process was used to prepare the Br-doped hollow TiO2 photocatalysts on the carbon sphere template following calcination at 400 °C (Wang et al. 2017). Novel ammonia and triethanolamine assisted sol-gel synthesis method was developed to fabricate the N-doped TiO_2 hollow spheres (Qiao et al. 2010). SiO_2@TiO_2 yolk-shell hollow nanospheres (STNSs) are outstanding photocatalysts due to their tunable structure and composition. Based on this point, unprecedentedly excellent photocatalytic properties of STNSs toward tannic acid via a Fe-N co-doped strategy were presented (Wan et al. 2018). Polystyrene@titanium dioxide (PS@TiO_2) composite with a different size was calcined at designated temperature, TiO_2 hollow sphere with controllable size was obtained for high efficient photo-reduction of Cr(VI) (Cai et al. 2017).

2.7 The effect dopants on TiO_2 for different uses

It has also been reported that the doping of the TiO_2 crystallites with metal and nonmetals could narrow its bandgap and shift its optical response from the ultraviolet to the visible-light region. The electrons injected into CB from VB can be easily transported to the catalyst's surface. Electrons can be easily trapped by doping with transition metals, noble metals, other metals, rare earth elements. Doping with metallic cations enhances the redox potential of the radicals generated during photocatalysis and reduces the e^- / h^+ recombination lifetime. In metal-doped TiO_2, the cations replace titanium atoms; meanwhile, in the non-metal-doped TiO_2, the anionic dopants are expected to substitute the oxygen atoms, although cationic substitutions may take place with some non-metals. As we can see on Ag/TiO_2 (Saravanan et al. 2018), Fe/TiO_2(Anwar and Mulyadi 2015), Se/TiO_2 (Xie, Li, and Xu 2018), N/TiO_2 (Li 2016), Gd/TiO_2 (Singh et al. 2019), Nd/TiO_2 (Shogh et al. 2015), Au/TiO_2 (Shi et al. 2017), Pt/TiO_2 (Song et al. 2019), Eu/TiO_2 (Zhuang, Zhou, and Liu 2013), N/TiO_2 (Qiao, Chen, and Wu 2010), Ni/TiO_2 (Wang et al. 2016), C/TiO_2 (Lu et al. 2017), Br/TiO_2 (Wang et al. 2017), Cr/TiO_2 (Yin and Zhao 2006), La/TiO_2 (Peng et al. 2015), Yb/TiO_2 (Jiang et al. 2017), Sn/TiO_2 (Li and Zeng 2007), Cu/TiO_2 (Kamble et al. 2018) were reported. The studies also investigated the different applications of the photocatalysts and the bandgap change and efficiency difference as compared to TiO_2 powder. A dopant can act as an effective mediator of interfacial charge transfer, inhibiting the electron-hole recombination or producing the opposite effect. Despite an extended response in the visible range, metal ions can act as recombination centers, decreasing the photocatalytic activity of the catalyst.

2.8 Photodegradation of MB using Fe doped TiO_2 photocatalyst

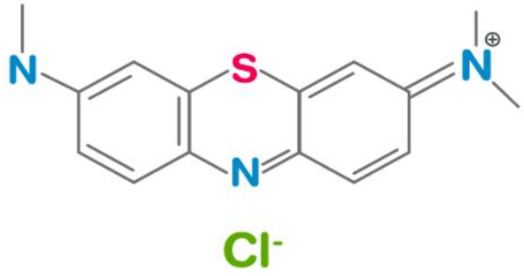

Figure 2. 2 Chemicals structure of Methylene blue.

Fe doped TiO_2 has been reported for the photodegradation of methylene blue (Anwar and Mulyadi 2015). It was reported that at 6wt% of the dopant and pH 10, 36% degradation without irradiation and 99.5% under visible light irradiation for 3 hours.

Monodisperse, multifunctional metal-ion-doped TiO_2 hollow particles have been reported in (Peng et al. 2009) that were synthesised by a general chemical method to tune the bandgap of titania by comparing different metal- ion doping, which uses polystyrene spheres as templates. Co-doped TiO_2

hollow particles, Fe-doped TiO_2 hollow particles, Co/Al-doped TiO_2 hollow particles, and Co/Zn-doped TiO_2 hollow particles display brilliant colours in the visible range, low reflectance in the ultraviolet range, and high infrared emissivity during in the range 8-14 µm.

Graphene wrapped Fe^{3+}- doped TiO_2 (Shi et al. 2018) composite was reported with high photocatalytic activity through a simple hydrothermal treatment combined with sol-gel method performed higher photo-degradation efficiency toward MB in comparison to TiO_2 and G- TiO_2 -Fe.

This study basically focuses on enhancing the morphology and electronic structure of TiO_2 to improve photocatalytic activity towards the degradation of MB via visible light irradiation. Iron doped TiO_2 hollow and porous nanospheres are prepared with a melamine-formaldehyde (MF) sphere as a polymer sacrificial template. The spheres are synthesised through hydrothermal polymerization, and Cetyltrimethylammonium bromide (CTAB) is used as a pore directing agent. Fe with different concentrations is doped on TiO_2 coated on MF sphere using sol-gel and calcination process. The effect of calcination temperature, catalyst loading, pH, dye concentration, and reusability are studied.

CHAPTER THREE

3. MATERIALS AND METHODS

3.1 Materials

Formaldehyde (HCHO, 37%) was obtained from LOBE chemi Pvt. ltd, India; Melamine (1,3,5-triazine-2,4,6-triamine; $C_3H_6N_6$,99%) were from DAEJUNG chemicals and metals, Korea; Formic acid (CH_2O_2, 85%) was obtained from Sigma- Aldrich, Germany; Absolute ethanol (99.9%), Cetyl trimethyl ammonium Bromide (CTAB, $C_{19}H_{42}BrN$, 98.98%) were from Sisco research laboratories Pvt. ltd, India; Iron chloride hexahydrate ($FeCl_3 \cdot 6H_2O$,99%) were from Biochem chemopharama, France. Titanium tetra-n- butoxide ($(CH_3CH_2CH_2CH_2O)_4Ti$, 97%) were from Kanto chemical co., inc, Japan, and Methylene blue, Distilled Water was used.

3.2 Methods

3.2.1 Synthesis of MF sphere

The MF (Melamine-Formaldehyde) spheres were prepared via hydrothermal polymerization as reported by the literature (Hao et al. 2020) with minor modifications. Briefly, 18.15 ml of formaldehyde solution (37%) was added into 400 ml of deionized water under stirring and heated to 80 ℃. Then, 5 g of melamine was utterly dissolved in the solution with stirring for pre-polymerization, and 0.4 ml of formic acid was introduced to the vigorously stirred solution until pH=5, then the transparent solution turned turbid. After additional agitation of the solution for 60 min, white MF spheres were obtained by centrifugation, washed three times with deionized water, and dried in air at 70 ℃.

3.2.2 Coating MF sphere with Fe doped TiO_2

0.4 g of MF spheres were dispersed homogeneously into 50 ml of absolute ethanol by sonicating the mixture for 30 min with a high-power sonicator. Then the MF ethanol suspension was transferred into a round-bottomed flask. A solution containing 0, 0.25 wt%, 0.5 wt%, and 1 wt % of Fe from Iron (III) chloride hexahydrate, 1 ml of water, and 0.06 g of Ceryltrimethyl ammonium bromide (CTAB) were added to the MF suspension solution at room temperature under magnetic stirring. After that, titanium tetra-n-butoxide was dissolved in 10ml ethanol to form a clear solution, then added to the above mixture dropwise. The reaction was allowed to sustain for 6 hours at 80 °C under continuous stirring. The solid product was then separated from the suspension by centrifugation and washed three times with distilled water and ethanol. Finally, the solid was re-dispersed into an appropriate volume of deionized water and cooled to freeze. White powder denoted as MF@CTAB-TiO_2 will be obtained after the freeze-drying process on a freeze-dryer, as reported on (Li 2016).

3.2.3 Preparation of Fe doped hollow and porous TiO_2 nanospheres

TiO_2 hollow and porous nanospheres were obtained via calcining MF@CTAB, Fe doped, and undoped TiO_2 composite by removing the MF cores and the pore-directing agents. The thermal treatments were performed with a programmed muffle furnace at 450, 500, 550 °C for three hours in the air.

Table 1-List of chemicals prepared, amount of chemicals used for synthesis, and Fe/TiO_2 molar ratio.

Photocatalyst	$FeCl_3.6H_2$0 Amount [mg]	Titanium tetra-n-butoxide $(CH_3CH_2CH_2CH_2O)_4Ti$ [mL]	Absolute ethanol [mL]	Mol ratio of Fe/TiO_2 [mol/mol]
Undoped THPNs	0	25	50	0
0.25% Fe-THPNs	0.25	25	50	0.0007
0.5% Fe-THPNs	0.5	25	50	0.02
1% Fe- THPNs	1	25	50	0.04

3.3 Photocatalytic test

The photocatalytic performance of Fe-THPNs was estimated by the degradation of Methylene blue (MB). First, 40 mg catalyst was ultrasonically dispersed in 100 ml of MB solution with a concentration of 10 ppm. Then it was stirred for 30 min in the dark to achieve an adsorption-desorption equilibrium. Then, the solution was exposed to the 150 W Halogen visible light lamp. Finally, the suspension was irradiated with a continuous stir in the photoreactor under magnetic stirring. In each, 15 min irradiation time interval, 5 ml of the sample was taken out and centrifuged at 4000 rpm for 15 min to separate the dye and catalyst solution.

3.4 Characterization

A thermogravimetric-differential thermal analyzer (TGA-DTA) (SHIMADZU DTG-60H) was used to determine the calcination temperature at which removal of MF templet and CTAB. The crystal structure and phase composition (phase purity) of the synthesized samples were determined by using XRD (SHIMADZU XRD -7000), in the 2θ range of 20-80º generated by a voltage of 40 kV and filament current 30 mA radiating CuKα^{-1} radiation (λ= 1.5418 A). Fourier transform infrared (FT-IR), Spectrum 65 FT-IR (PerkinElmer) in the range 4000-400 cm^{-1} (resolution: 4 cm^{-1}, number of scans:4) using KBr pellets was used to analyze the chemical composition of the samples. For liquid samples KBr windows was used. The samples' structure, morphologies, and elemental composition analysis were analyzed using Scanning Electron Microscopy/Energy Dispersive Spectroscopy (SEM/EDS). Uv-Visible spectroscope (UV-3600Plus) was used to measure the absorbance of the MB dye after the photocatalytic experiment. Surface area, pore size and pore volume were analyzed using BET surface area analyzer. Zeta sizer (Zetasizer Ver. 7.11, MAL1149420) was used to determine the particle size of the sample.

CHAPTER FOUR

4 RESULT AND DISCUSSION

4.1 Thermal analysis

In Figure 4.1(red curve), Differential Thermal Analysis (DTA) result is presented. As a result of the temperature difference between the sample (Fe-doped THPNS) and the reference material (MF sphere), both exothermic or endothermic changes were observed. A phase change occurs in the endothermic reaction through decomposition, fusion, vaporization, sublimation, and melting. The broadening of the peak occurs at 85.24 °C indicates the endothermic reaction obtained from dehydration reaction. In contrast, crystallization, oxidation, and chemical sorption occurred in the exothermic process at 266.04 °C, 422.78 °C, and 529.33 °C since heat is evolved by the sample.

Thermogravimetric analysis (TGA) measures the mass of a sample as it is heated, cooled, or held at a constant temperature in a defined atmosphere. The result obtained is presented in Figure 4.1 **(**blue curve). TGA determines a material's thermal stability, its fraction of volatile components, purity, decomposition reactions, and composition by monitoring the weight change as a sample is heated at a constant rate. Around 49% of the mass reduction was observed till the temperature gets 800 °C. The first phase shows evaporation of adsorbed water, volatile compound removed, and MF sphere decomposed since the total weight used for the measurement reduced from 13.762 to 4.458 mg (-32.394%) at below 100 °C. The second phase, around 100 to 300, indicates there is no mass change. Around 400 to 600 °C, a weight loss appears (-2.374 mg) when the atmosphere changes from nitrogen to air. The other phase indicates an inert organic residue of ash (Liu et al., 2019).

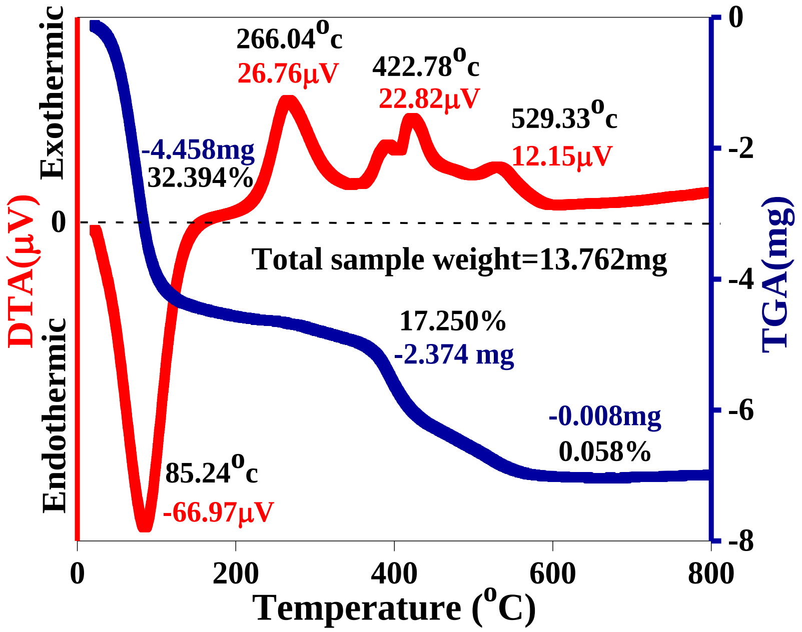

Figure 4. 1 TGA-DTA graph of chemical synthesized using MF template and Fe doped THPNS.

4.2 DRS analysis

The data obtained from Uv–Vis reflectance spectra were used to evaluate the bandgap energy of TiO_2 and Fe-doped TiO_2 photocatalysts using Kubelka Munk function (F(R)).

$$\mathbf{F(R)} = \frac{\mathbf{k}}{\mathbf{S}}, \qquad \mathbf{k= (1\text{-}R)^2}, \qquad \mathbf{S= 2(R)}$$

Where **k** is the molar absorption coefficient, **S** is the scattering factor, **R** is the reflectance of a material. Figure 4.2 shows Fe doping on TiO_2 significantly influences the bandgap energy value. As the curve indicates at 0.25 and 0.5wt% of Fe amount, the bandgap energy decreased from 3.47 eV (undoped THPNS) to 3.25 eV, and 3.27 eV observed; However, at 1wt% of Fe doped TiO_2, the bandgap (3.59 eV) is higher than undoped THPNS. The bandgap energy value of Fe-doped TiO_2 samples indicated their potential photoactivity under light irradiation.

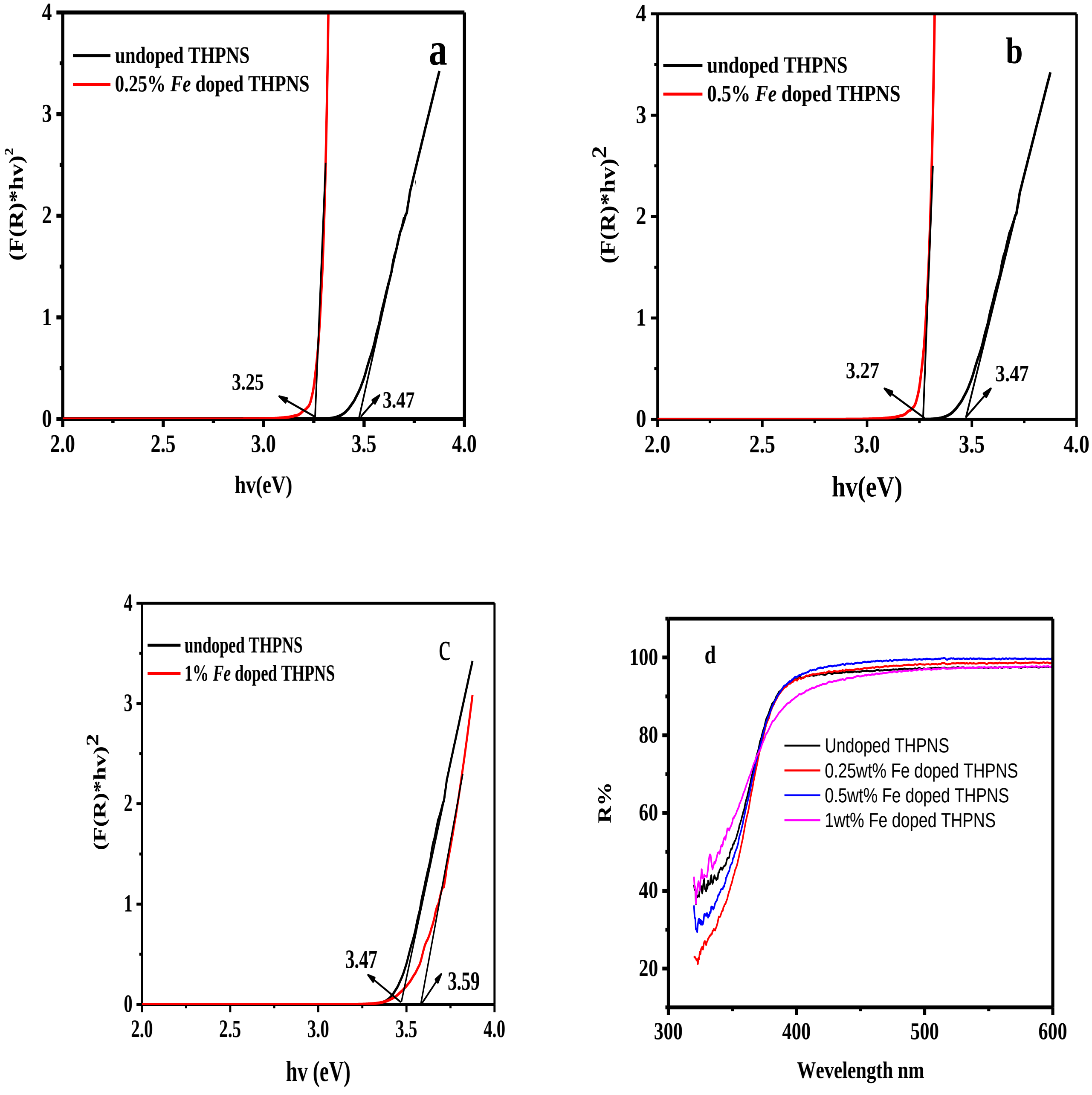

Figure 4. 2 Bandgap evaluation of undoped and doped THPNS (a) 0.25wt% Fe (b) 0.5wt% Fe (c) 1wt% Fe doped THPNS (d) R% vs wavelength.

4.3 XRD analysis

Figure 4.3(a) shows the XRD patterns of Fe-THPNS with different Fe doping ratios. The typical diffraction peaks of Fe-THPNS had no other peaks compared to the standard card data of anatase phase TiO_2 (JCPDS No. 21-1272). The diffraction peak observed at $2\theta=25^o$, 38^o, 48^o, 54^o, 62^o, 69^o, and 75^o at (101), (004), (200), (211), (204), (220), and (215). The outcomes directed that either the Fe content of the sample is lower than the detection limits of the XRD instrument or the Fe ions doped into the TiO_2 structure at a low concentration. The peak width depends on two factors; the crystallite size and lattice strain.

The crystallite sizes of the samples at the anatase diffraction peaks, calculated by Debye- Scherer equation, $\mathbf{D} = \frac{\mathbf{k\lambda}}{\mathbf{B*cos(\frac{\theta}{2})}}$ showed a clear difference (Shen et al. 2012).

Where D is the crystallite size (nm), B is the peak full-width at half maximum after correction of the instrumental broadening (rad), λ the wavelength (nm), and θ the Bragg angle (rad). Both the diffraction angle and the full width at half maximum of the samples changed to some extent after doping showed in Table 2; the crystallite sizes reduced due to the presence of Fe. The undoped TiO_2 has a larger crystallite size than that of the doped TiO_2, compared to those doped TiO_2, 0.25% Fe doped has the smallest crystallite size. The main reason was that Since the ionic radius of the Fe^{3+} ion (0.064 nm) is smaller than the Ti^{4+} ion (0.068 nm), and considering that the Pauling electronegativity of Fe^{3+} (1.83) and Ti^{4+} (1.54) are similar, Fe^{3+} ions may enter the crystal cell of TiO_2 at substitutional sites as stated in (Zuorro et al. 2019). Figure 4.3(b) shows the diffraction peak at (101) crystal plane of Fe-THPNS samples at different iron concentrations. Figure 4.7.5(a) shows the effect of calcination temperature at 450, 500, and 550^OC. The change affects the crystallite size corresponding to that of the anatase phase of TiO_2. The undoped and Fe doped THPNS crystallinity is around 90 – 91% calculated using peak to noise ratio.

Crystallinity or Peak to noise ratio = $\frac{\textbf{Area of crystalline peaks}}{\textbf{Area of all peaks}} * 100.$

The TiO_2 lattice is not deformed by Fe doping as we can see from Lattice constant **a=b** and **c,** Fe doped and undoped THPNS has a tetragonal crystal structure (Mital and Manoj 2011) and pure anatase phase.

Table 2 Crystallite size, %Crystallinity, and Lattice constant of the prepared photocatalysts.

Photocatalyst	Crystallite size (nm)	% Crystallinity	a	c
			Lattice constant	
Undoped THPNS	10.24	91.6	3.788	9.43532
0.25% Fe doped THPNS	6.44	90.75	3.775	9.44248
0.5% Fe doped THPNS	8.84	92.27	3.791	9.4628
1% Fe doped THPNS	8.24	91.58	3.789	9.483

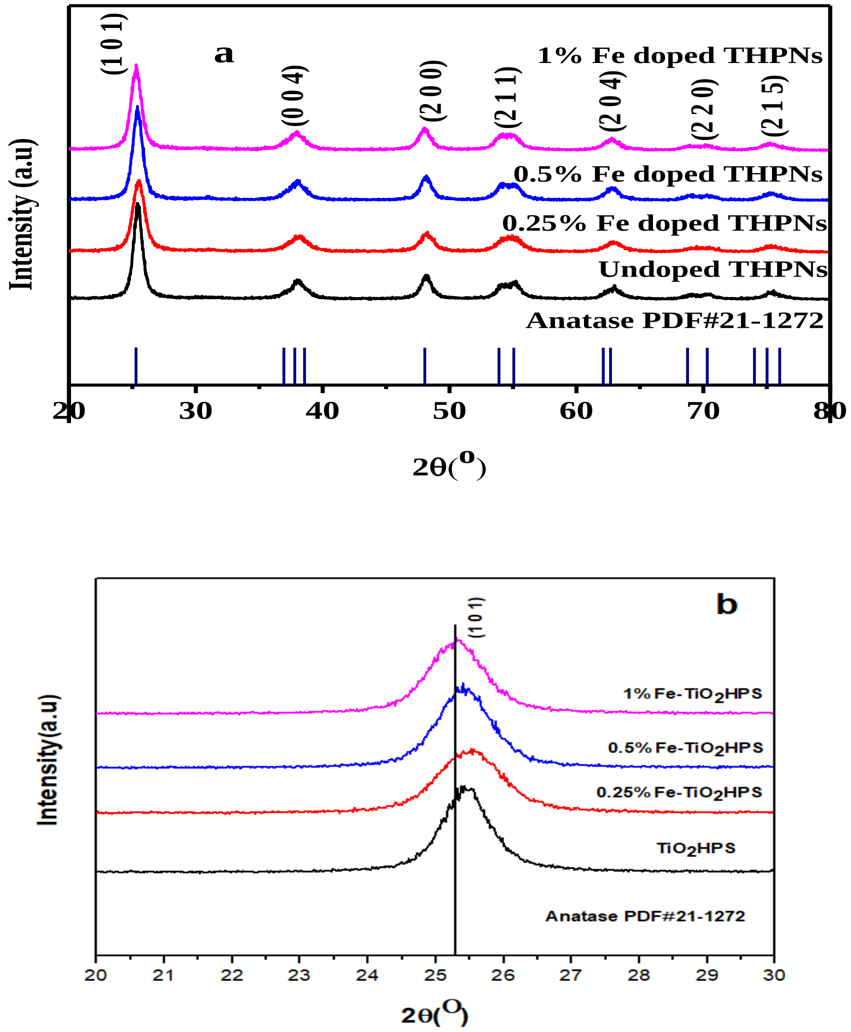

Figure 4. 3 XRD patterns of undoped and Fe doped TiO2 (a), and (b) diffraction peaks at (101).

4.4 FT-IR analysis

As revealed in Figure 4.4.1 (a), the typical spectrum of MF nanosphere, the peaks of -NH_2 vibration (1564 cm^{-1}, 1494 cm^{-1}, 1343 cm^{-1}), -OH/-NH- vibration (3371 cm^{-1}, 2956 cm^{-1}), C-N vibration (1162 cm^{-1}), C-O-C vibration (1003 cm $^{-1}$), and C-N-C vibration (810 cm^{-1}) may specify that the synthesis of MF templates was successful (Liu et al. 2012). FTIR spectra of uncalcined Fe-THPNS and THPNS are presented in Figure 4.4 (b) and (c). TiO_2@MFC shows a similar FT-IR spectrum compared with MF, but the intensities of several peaks such as the peaks of ether vibration (3406cm^{-1}, 1557 cm^{-1}, 1350 $cm^{-1,}$ and in addition 2921 cm^{-1} for the doped THPNS) decreased. The cause of these intensity variations was that the MF templates were coated with the TiO_2 particles (Jiang et al, 2017). In Figures 4.4.1 (d) and (e), the spectra show the complete removal of the MF template. A weak peak shows a sign of incorporated nitrogen in the C-TiO_2 sample, appears at 941 cm^{-1} and 1633 cm^{-1} directs CO_2 absorption in air. The FTIR results support the formation of the MF@CTAB-TiO_2 core-shell composite intermediate after the sol-gel coating process and the formation of the hollow and porous TiO_2 product after calcination (Li 2016).

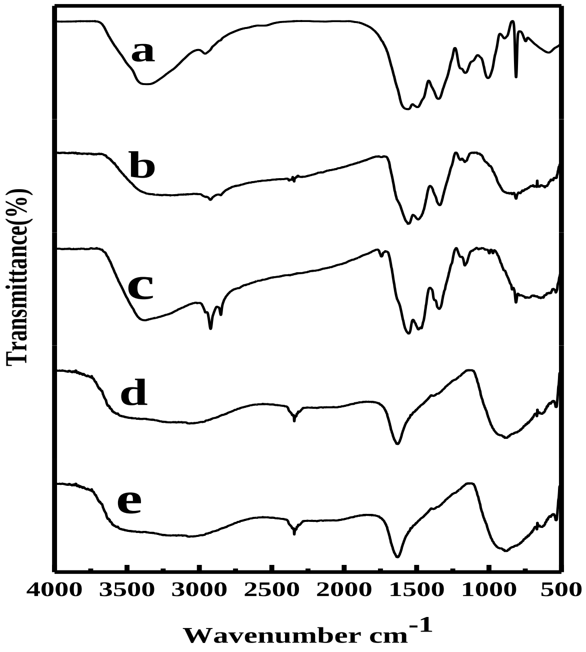

Figure 4. 4 FT-IR images of (a) pure MF sphere, (b and c) MF@CTAB undoped and Fe doped TiO2, (d and e) Fe doped and undoped THPNS.

FT-IR analysis of MB was carried out before and after the photocatalytic degradation. To endorse the final product formation and understand the photocatalytic reaction path of MB dye degradation via Fe doped THPNS under Visible light irradiation. As Figure 4.4.1 shows, 3399 cm^{-1} is assigned to the stretching vibration mode of the structure, or (surface) hydroxyl groups chemisorbed, 2090 cm^{-1}, 1640 cm^{-1} is assigned to water molecules. The peak below 1000 cm^{-1} corresponds to the titania crystal lattice vibration. In contrast, the FTIR spectrum of pure MB shows more complicated vibrational modes due to the organic molecule. For pure methylene blue, the peak appears at 2983 cm^{-1} and near represents the stretching vibration of −CH− aromatic and $–CH_3$ methyl groups. The spectra ranging from 1640 cm^{-1} to 1398 $cm^{-1}$are assigned to the aromatic ring structures in methylene blue. The peak at 1045 cm^{-1} is related to the C=C skeleton of the aromatic rings. The spectra indicate that MB degrades using Fe- doped THPNS since almost all peaks disappeared on the fingerprint region, and there is a slight difference in the width.

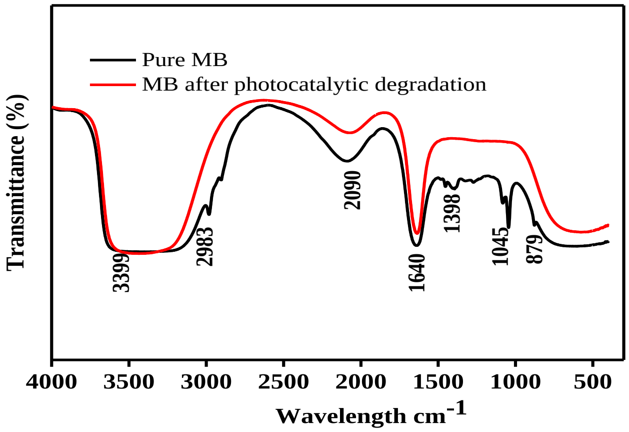

Figure 4.4 1 FT-IR spectra of pure MB and photocatalytic removal of MB.

4.5 SEM analysis

Figure 4.5 (A) shows that the MF sphere was successfully prepared via hydrothermal polymerization using melamine and formaldehyde. SEM image demonstrated that the MF template showed a smooth surface texture with a particle size of MF sphere is 955± 72 nm as indicated in Zeta sizer result **Figure 4.5 (B).** Furthermore, the SEM image is shown in **Figure 4.5 (C)** indicates Fe doped THPNS successfully synthesized through sol-gel and calcination process of particle size 107±18 nm as indicated in **Figure 4.5 (D)** of zeta sizer result. The existence of Fe in this sample was confirmed by the EDS spectrum in Figure 4.5 (E). The EDS result also demonstrates that only the elements of C, O, Fe, and Ti are contained in the sample, and the atomic percentages are 45.18, 42.37, 12.47, and 0.02%, respectively.

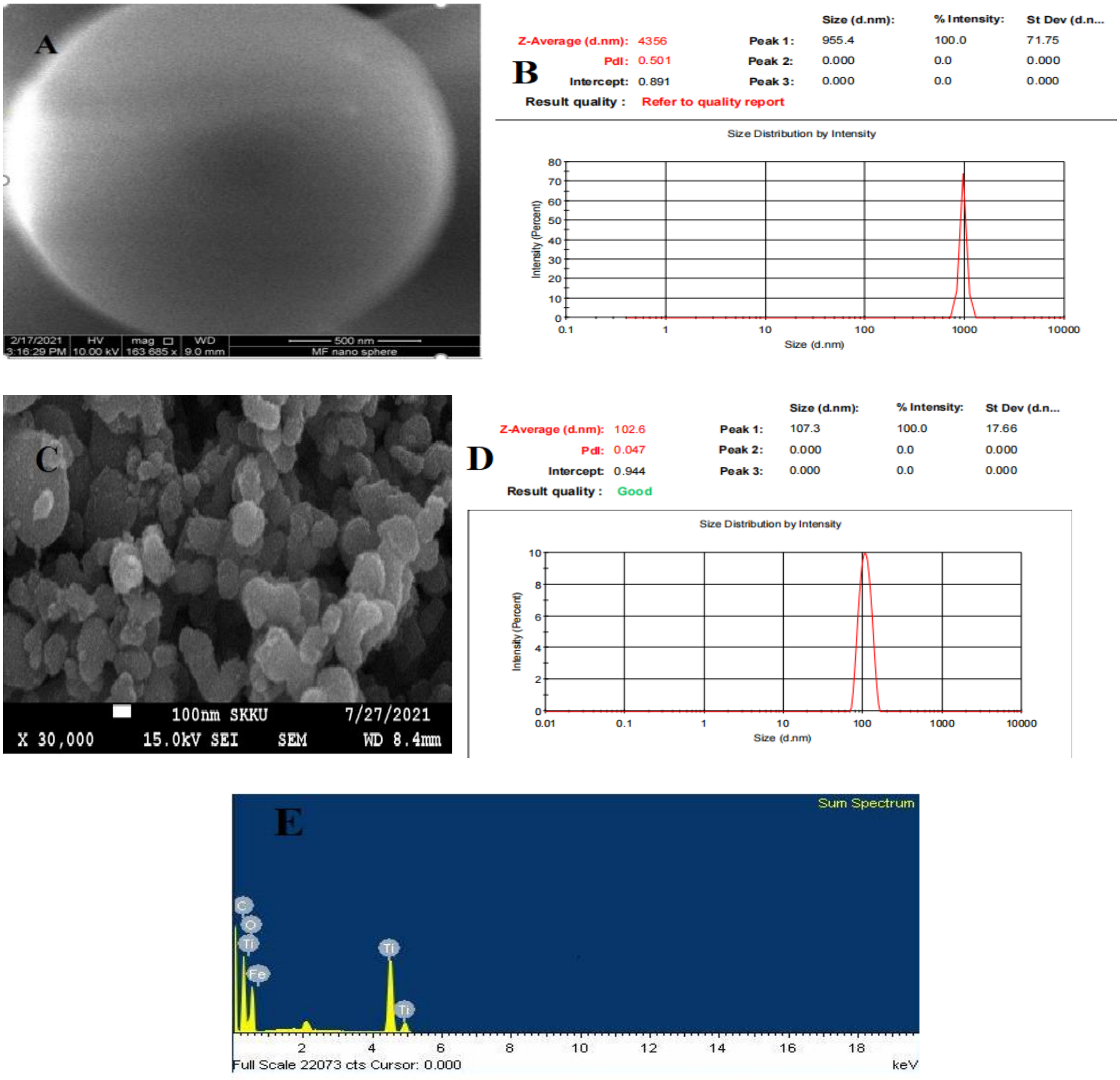

Z-Average (d.nm): 4356
PdI: 0.501
Intercept: 0.891
Result quality : Refer to quality report

	Size (d.nm):	% Intensity:	St Dev (d.n...
Peak 1:	955.4	100.0	71.75
Peak 2:	0.000	0.0	0.000
Peak 3:	0.000	0.0	0.000

Z-Average (d.nm): 102.6
PdI: 0.047
Intercept: 0.944
Result quality : Good

	Size (d.nm):	% Intensity:	St Dev (d.n...
Peak 1:	107.3	100.0	17.66
Peak 2:	0.000	0.0	0.000
Peak 3:	0.000	0.0	0.000

Full Scale 22073 cts Cursor: 0.000

Figure 4. 5 SEM image shows the morphology, and Zetasizer indicates the particle size, (A) SEM image of MF sphere (B) particle size of MF sphere (C) SEM image of 0.25wt% Fe doped THPNS, (D) particle size Fe doped THPNS, (E) EDS image of Fe doped THPNS.

4.6 BET surface area analysis

To better understand the structures for the materials, N2 adsorption desorption isotherms were performed. Both of the N2 adsorption desorption isotherms are typical type II curves, indicating the existence of micro pores in the materials. The micropores in both are less than 2nm in diameter using Horvath-Kawazoe Method (HK) and Saito-Foley Method (SF) method cumulative pore volume and pore size. The Brunauere Emmett Teller (BET) surface area of undoped THPNS and Fe doped THPNS composites are 345.8 m2 g^{-1} and 368.756 m2 g^{-1}, respectively.

Table 3 BET surface area, pore size and pore volume of doped and undoped THPNS.

Sample	Surface area(m^2g^{-1})	Pore size(nm)		Pore volume (cc/g)	
		SF	HK	SF	HK
Undoped THPNS	345.8	1.721	0.9237	9.830e-02	8.954e-02
Doped THPNS	368.756	0.2261	0.18838	1.267e-02	1.175 e-01

4.7 Uv-Vis analysis

4.7.1 Effect of Iron concentration

Initial experiments were made to estimate whether a photocatalytic treatment could degrade MB. In these experiments, the photodegradation process was carried out using the 10 ppm concentrations of the dye in 100 ml, 0.04 g load of the catalyst, and pH of 7 for an overall duration of two hours (30 minutes of darkness and 90 min of irradiation). The following catalysts were tested; undoped and Fe-doped HPTNs at three Fe levels: 0.25wt% Fe-HPTNs, 0.5wt% Fe-HPTNs, and 1wt% Fe-HPTNs as indicated on Appendix 1, 2, and 3. The degradation efficiency is calculated by $\boldsymbol{\eta} = \frac{\mathbf{Ct-Co}}{\mathbf{Co}} * 100$ the equation, where Co is the Absorbance of MB solution at 10 ppm and Ct is the Absorbance of the degradation of MB solution after light irradiation in each 15 min interval using Fe doped hollow and porous TiO_2 sphere. Figure 4.81 indicates a slight difference in the efficiency of 0.25 wt% Fe calcined at 450 °C shows a higher degradation efficiency than the others. The photodegradation process of dye shows an apparent pseudo-first-order kinetics equation as indicated on Appendix(5). Where k is the apparent pseudo-first-order rate constant, Co is the primeval MB concentration, and Ct is MB solution concentration at time t (Mishra and Mukhopadhyay 2019).

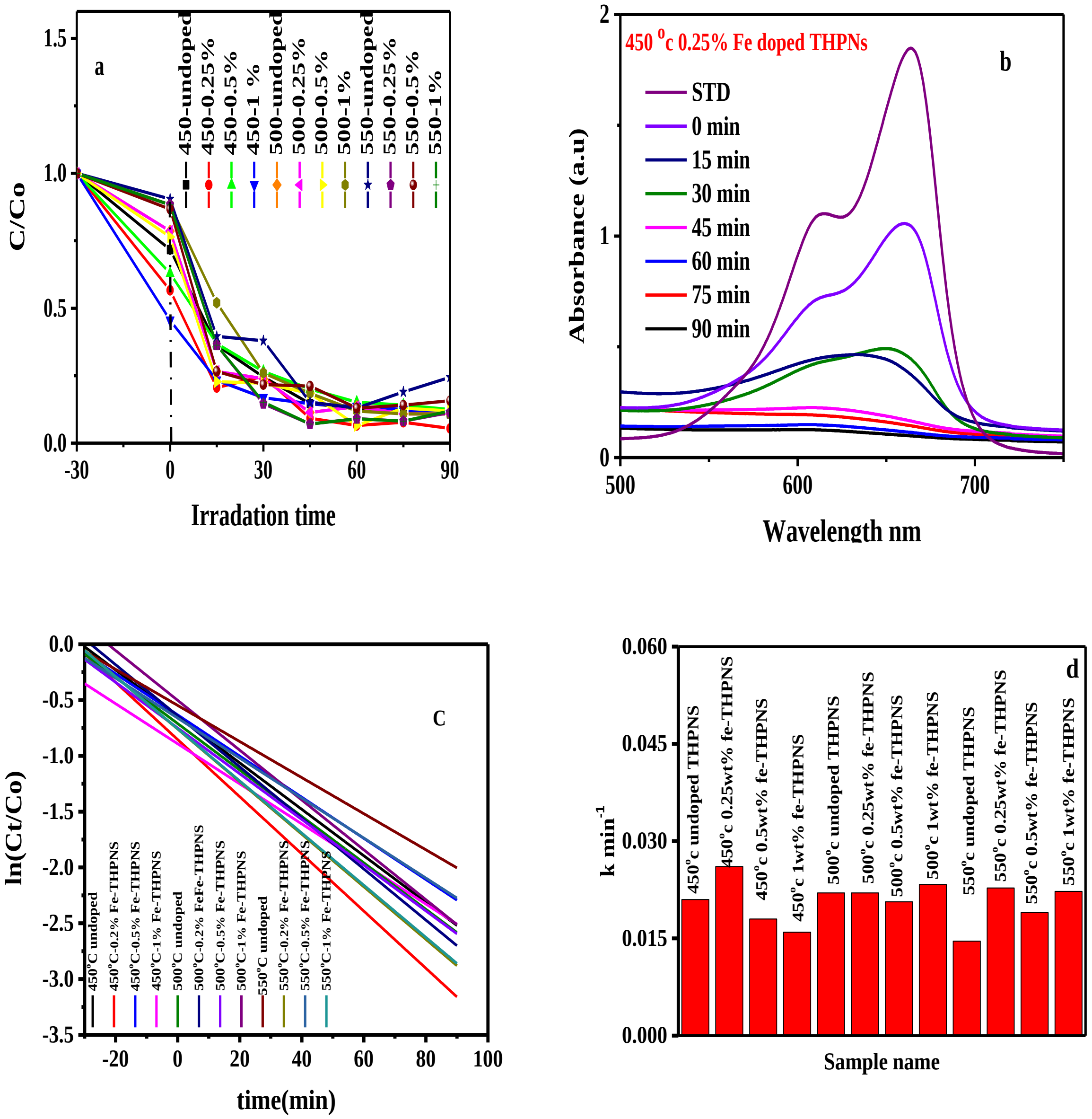

Figure 4.7 1 (a) phoocatalytic activity of the synthesized sample, (b) absorbance vs wavelength graph of 0.25wt% Fe-THPNS at 450oC, ln(Ct/Co) vs time, and (d) Kinetics for the removal of MB for the synthesized sample.

Table 4 Photocatalytic efficiency, rate constant from 1st order reaction (k), and regression (R^2) of the synthesized samples.

Sample	**Annealing temperate, °C**	**Dopant concentration**	**Rate constant, K, min^1**	**Regression R^2**	**Photocatalytic removal efficiency, (%)**
Pure THPNS	450	Undoped	0.020993	0.92259	89
Pure THPNS	500	Undoped	0.022011	0.84548	89
Pure THPNS	550	Undoped	0.01457	0.65496	76
0.2% Fe-THPNS	450	0.2	0.026074	0.90889	94
0.2% Fe-THPNS	500	0.2	0.022011	0.92086	91
0.2% Fe-THPNS	550	0.2	0.022769	0.73042	88
0.5% Fe-THPNS	450	0.5	0.017979	0.95533	87
0.5% Fe-THPNS	500	0.5	0.020641	0.74825	88
0.5% Fe-THPNS	550	0.5	0.018977	0.7813	84
1 % Fe-THPNS	450	1	0.015945	0.85727	89
1 % Fe-THPNS	500	1	0.023311	0.9155	89
1 % Fe-THPNS	550	1	0.022252	0.72276	88

4.7.2 Effect of Dye Concentration

The chance of forming active sites on the catalyst surface and radicals reacting with dye molecules determine the degradation rate. As the initial dye concentrations increase, more dye molecules are present for excitation and energy and provides the formation of several monolayers of adsorbed dye on the TiO_2 surface; this leads to a decrease in the degradation efficiency of the catalyst. A significant amount of light is absorbed by the dye molecules rather than the TiO_2 particles; the penetration of light to the catalyst's surface decreases, and it leads to a reduction in the generation of hydroxyl radicals or photocatalytic degradation. On the other hand, the adsorbed dye on the photocatalyst also inhibits the reaction of adsorbed molecules with the photo-induced positive holes or hydroxyl radicals since there is no direct contact of the semiconductor with them. This reduces the path length of the photons entering the solution. Again, as the initial concentration of the dye increases, the requirement of catalyst surface and irradiation time needed for the degradation also increases. Since illumination time and amount of catalyst are constant, the radical (primary oxidant) formed on the surface of TiO_2 is also constant. So the relative number of free radicals attacking the dye molecules decreases with an increasing amount of the dye. The effect of dye concentration is studied at a constant catalyst loading of 40 mg and pH=7 for an overall duration of two hours with 5, 10, and 15 ppm dye concentrations in 100 ml volume of dye solution. The result is shown in **Figure 4.7.2.** As the dye molecules concentration increases, the efficiency of the photocatalyst is reduced.

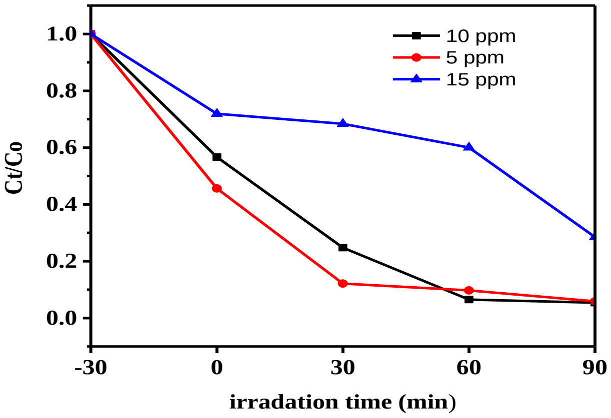

Figure 4.7 2 Effect of dye concentration on photocatalytic removal of MB.

4.7.3 Effect of catalyst loading

The amount of catalyst used in the photocatalytic treatment is another essential factor for optimizing the degradation of pollutants. The effect of catalyst loading was evaluated at 20, 40, and 60 mg/L keeping the pH at seven and the initial dye concentration at 10 ppm of 100 ml sample volume. The results of these experiments are shown in **Figure 4.7.3.** From the plot, it is possible to state that as the catalyst load increases, removal efficiency increases. The efficiency improvement is due to the increase in the interaction of light and the catalyst that produces more photogenerated holes and electrons and free radicals.

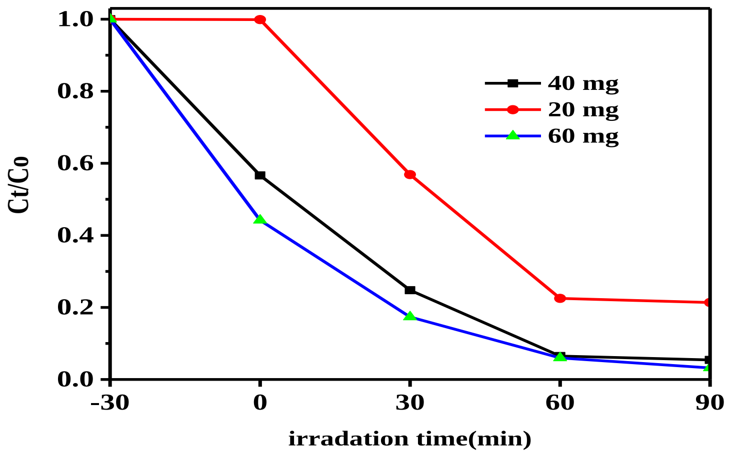

Figure 4.7 3 Effect of catalyst loading on the photocatalytic removal of MB.

4.7.4 Effect of pH

The effect of pH on the photocatalytic efficiency of the samples was studied by varying the pH of the dye solution since the effluent discharged from the industries could be at different pH values. The experiment conducted for the removal of the MB in acidic media was at a pH of 2, while the basic media was at a pH of 11, and the dye at neutral (pH =7) condition was carried out to investigate the effect. The initial dye concentration was set at 10 ppm of 100 ml and the catalyst load was 0.04 g. The results were obtained during a two-hour treatment period (30 minutes of darkness and 90 minutes of irradiation). As shown in **Figure 4.7.4,** the removal efficiency of MB in the basic solution is much higher than in other cases. Evidence from previous studies indicated that pH could affect the photocatalytic removal of dyes in multiple ways, as it may influence the surface properties of the catalyst, the charge distribution on the dye molecule, and the generation of reactive radical species. The influence of pH on dye removal can be attributed to its effects on the generation of radical species during the photocatalytic process. These radicals are produced at the catalyst surface from the oxidation of OH or H_2O by the photogenerated holes (h^+).

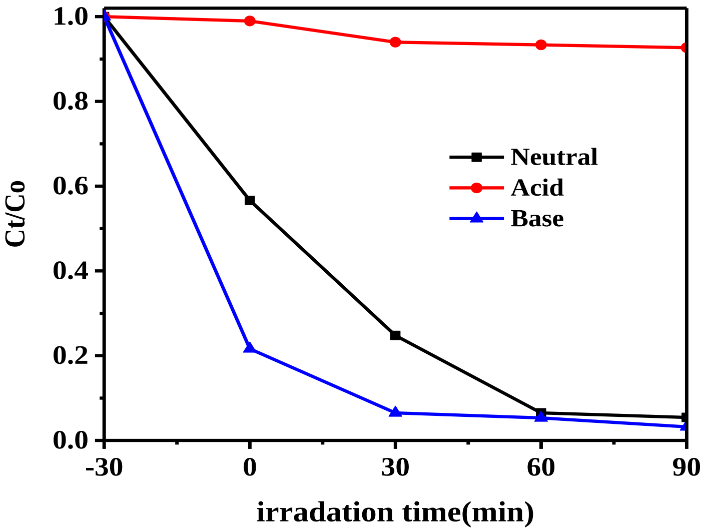

Figure 4.7 4 Effect of pH on the photocatalytic removal of MB.

4.7.5 Effect of calcination temperature

At constant catalyst loading (0.04 g), dye concertation (10 ppm), and pH of dye solution (pH=7), the effect of temperature is vividly seen. In **Figure 4.7.5(a),** the XRD result shows the peak width for 450 ^{o}C is higher than 500 and 550 cases. As the calcination temperature increases, those peaks associated with anatase phase TiO_2 become sharper, indicating that the higher calcination temperature promotes the forming of anatase TiO_2 of high crystallinity (Shen et al. 2012). The crystallinity, surface area, and porous size mainly depend on the calcination temperature. Therefore, calcination temperature affects the catalyst performance, as shown in **Figure 4.7.5(b).**

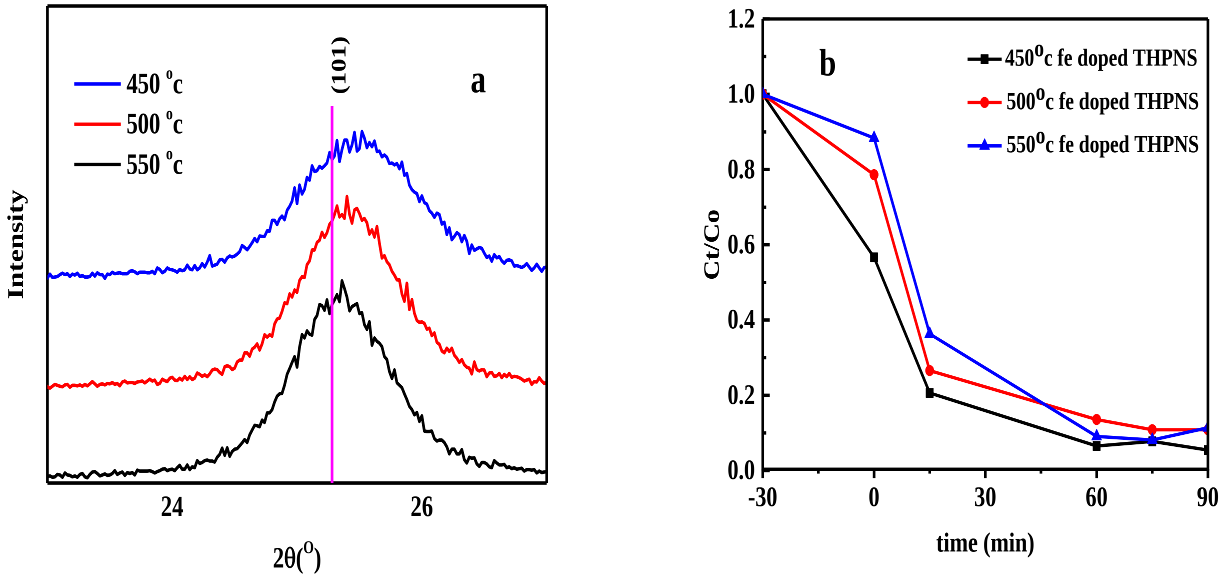

Figure 4.7 5 Effect of calcination temperature on photocatalytic removal of MB. (a) XRD image, and (b) removal activity.

Table 5 Effect of calcination temperature on crystallite size, and % crystallinity.

Photocatalyst	Calcination temperature, ^{O}C	Crystallite size, (nm)	% Crystallinity
Fe doped THPNS	450	8.851	90.75
Fe doped THPNS	500	8.848	92.27
Fe doped THPNS	550	8.68	91.58

4.7.6 Reusability

To determine the stability of the 0.25%Fe doped TiO_2 at 450 °C of 40 mg photocatalyst reusability experiment was carried out on the degradation of methylene blue with 10 ppm concentration of MB in 100 ml volume of the sample. Typically, after the first photodegradation reaction was completed, the photocatalyst was recovered by centrifugation. Then, the recovered photocatalyst was washed three times with distilled water to remove adsorbed MB and dried. After that, the dried photocatalyst was reused for the next photocatalytic reaction cycle as shown in the **Figure 4.7.6.** A slight decrease in the removal efficiency for the first three cycles was observed, while after the fourth cycle, the catalyst's efficiency reduced very rapidly. The reduction of the efficiency of the catalyst deteriorates due to the photo corrosion effect of the catalyst.

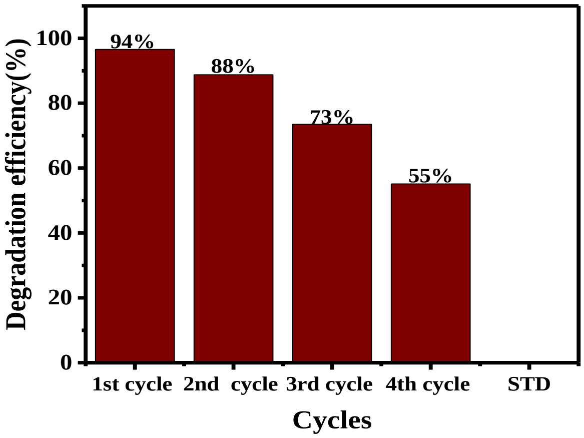

Figure 4.7 6 Reusability of photocatalyst in four cycle of MB removal.

4.7.7 Model formation Fe-THPNS

As shown in **Figure 4.7.7,** the synthesis of MF spheres with a size around 950 nm were prepared using Melamine and Formaldehyde through a hydrothermal polymerization process. The following picture is intended to describe TiO_2 coated on MF sphere and adds CTAB as a pore directing agent. Afterward calcination process occurs to remove CTAB, MF sphere, and to obtain crystalline anatase phase. As a result, indicated in the SEM **Figure 4.5(C),** we successfully synthesized iron-doped and undoped hollow and porous THPNS.

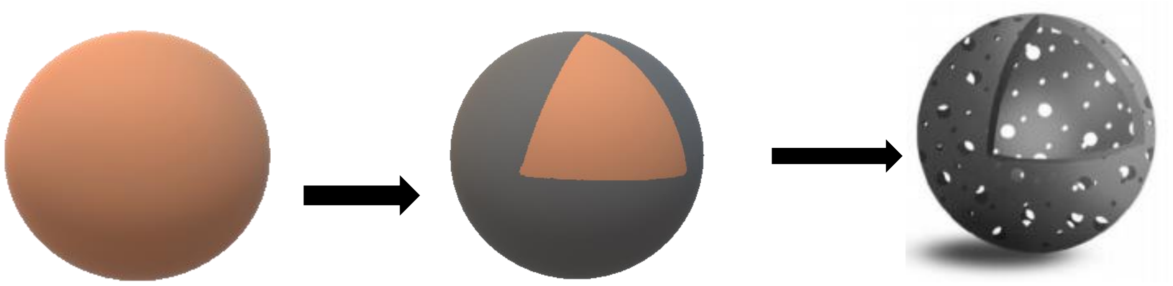

MF sphere | TiO_2 coated on MF sphere | Hollow and porous TiO_2

Hydrothermal polymerization | Sol-Gel Process | Calcination Process

Figure 4.7 7 Illustration of the formation process for THPNS.

CHAPTER FIVE

5 CONCLUSION AND RECOMMENDATION

5.1 Conclusion

- Iron doped and undoped titanium hollow and porous nanospheres (Fe-THPNS) were successfully prepared via a sol-gel and calcination process, utilizing melamine-formaldehyde (MF) spheres as a template and Cetyltrimethylammonium bromide (CTAB) as a pore directing agent.
- Fe doped TiO_2 has occurred in the anatase phase, which has good photocatalytic performance.
- Hollow and porous structures make TiO_2 have a larger surface area as indicated on the BET image (BET surface area increases from 345 m^2/g undoped THPNS to 368.756 m^2/g 0.25wt% doped THPNS), and pore size and pore volume reduced when the iron doped as indicated in Table 3, more surface-active groups, more comprehensive absorption range of light, and lower bandwidth which helps to improve the photocatalytic activity.
- Different iron dopant concentrations significantly affect photocatalytic activity due to the change in its bandgap from 3.4 eV to 3.2 eV. The change in crystallite size and microstrain also depends on the radius and the electronegativity of Fe^{3+} and Ti^{4+}. Fe substitute in the Ti place since the radius of the iron is lower than Ti.
- Compared to all samples, 0.25%Fe-THPNS at 450^{o}C showed the best catalytic performance (about 94%). Factors that lead to an increase in the degradation performance due to lower bandgap achieved from iron and higher surface area arise from the hollow and porous morphology of the synthesized TiO_2.

5.2 Recommendation

- In this thesis, only MB is selected as the target pollutants to evaluate the photocatalytic activity of the synthesized photocatalysts. In the future, the photocatalytic performance of other organic pollutants and real textile effluents can be investigated.
- Due to the limitation of materials, we can’t do further work on the degradation mechanism. It is better to study active species involved in photocatalytic reactions based on active species trapping experiments. Further work needed to reduce the bandgap of TiO_2 to trap light under visible light region.

REFERENCE

1. AL-Jawad, Selma M. H., Ali A. Taha, and Mohammed M. Salim. 2017. “Synthesis and Characterization of Pure and Fe Doped TiO2 Thin Films for Antimicrobial Activity.” Optik 142:42–53.

2. Bashiri, Robabeh, and Norani Muti Mohamed. 2017. “Advancement of Sol-Gel – Prepared TiO 2 Photocatalyst.” Advancement of Sol-Gel–Prepared TiO2 Photocatalyst 18.

3. Cao, Songjie, Zhe Xue, Chengwu Yang, Jiaqian Qin, Long Zhang, and Pengfei Yu. 2018. “Nano Energy Insights into the Li + Storage Mechanism of TiC @ C-TiO 2 Core-Shell Nanostructures as High-Performance Anodes.” Nano Energy 50(May):25–34.

4. Ding, Yong, In Seok Yang, Zhaoqian Li, Xin Xia, Wan In Lee, and Songyuan Dai. 2019. “Nanoporous TiO 2 Spheres with Tailored Textural Properties : Controllable Synthesis, Formation Mechanism , and Photochemical Applications.” Progress in Materials Science 100620.

5. Huang, Jiarui, Haibo Ren, Xiaosi Liu, Xuexue Li, and Jae Jin Shim. 2015. “Facile Synthesis of Porous TiO2 Nanospheres and Their Photocatalytic Properties.” Superlattices and Microstructures 81:16–25.

6. Jia, Xiaohua, Chuande Cheng, Shaopei Feng, Xiaojing Yu, Linxuan Xia, and Haojie Song. 2019. “Applied Surface Science Synthesis , Characterization , and Gas-Sensing Applications.” Applied Surface Science 481(November 2018):1001–10.

7. Jiang, Xueliang, Chenjian Li, Song Liu, Fuqing Zhang, Feng You, and Chu Yao. 2017. “RSC Advances The Synthesis and Characterization of Ytterbium- Doped TiO 2 Hollow Spheres with Enhanced.” 24598–606.

8. Kaygili, Omer, Niyazi Bulut, Cengiz Tatar, Tankut Ates, and Turan İnce. 2017. “Sol-Gel Synthesis And Characterization Of TiO2 Powder.” International Journal of Innovative Engineering Applications 1(2):38–40.

9. Li, Jing and Hua Chun Zeng. 2007. “Hollowing Sn-Doped TiO 2 Nanospheres via Ostwald Ripening.” (16):495–503.

10. Liu, Hui, Hongliang Li, Zhaolong Ding, and Aiping Fu. 2012. “Preparation of Porous Hollow SiO 2 Spheres ¨ Ber Process Using MF Microspheres by a Modified Sto as Templates.” 273–85.

11. Lum, P. T., K. Y. Foo, N. A. Zakaria, and P. Palaniandy. 2020. “Ash Based Nanocomposites for Photocatalytic Degradation of Textile Dye Pollutants : A Review.” Materials Chemistry and Physics 241(August 2019):122405.

12. Scholz, D. A. Yaseen M. 2018. Textile Dye Wastewater Characteristics and Constituents of Synthetic Effluents : A Critical Review. Springer Berlin Heidelberg.

13. Shen, H. L., H. H. Hu, D. Y. Liang, H. L. Meng, P. G. Li, W. H. Tang, and C. Cui. 2012. "Effect of Calcination Temperature on the Microstructure , Crystallinity and Photocatalytic Activity of TiO 2 Hollow Spheres." 542:32–36.

14. Singh, Rohini and Suman Dutta. 2018. "A Review on H2 Production through Photocatalytic Reactions Using TiO2 / TiO2- Assisted Catalysts Review Article A Review on H 2 Production through Photocatalytic Reactions Using TiO 2 / TiO 2 -Assisted Catalysts." Fuel 220(May):607–20.

15. Xu, Piao, Guang Ming, Dan Lian, Chong Ling, Shuang Hu, and Mei Hua. 2012. "Science of the Total Environment Use of Iron Oxide Nanomaterials in Wastewater Treatment : A Review." Science of the Total Environment, The 424:1–10.

16. Ye, Miaomiao, Zhonglin Chen, Wenshou Wang, Jimin Shen, and Jun Ma. 2010. "Hydrothermal Synthesis of TiO 2 Hollow Microspheres for the Photocatalytic Degradation of 4-Chloronitrobenzene." Journal of Hazardous Materials 184(1–3):612–19.

17. Yen, Yin-cheng, Jau-an Chen, Sheng Ou, Yi-shin Chen, and Kuan-jiuh Lin. 2017. "Plasmon-Enhanced Photocurrent Using Gold Nanoparticles on a Web Electrode." Nature Publishing Group (January):1–8.

18. Zada, Imran, Wang Zhang, Wangshu Zheng, Yuying Zhu, and Zhijian Zhang. 2017. "The Highly Efficient Photocatalytic and Light Harvesting Property of Ag-TiO 2 with Negative Nano-Holes Structure Inspired from Cicada Wings." Scientific Reports (November):1–9.

19. Zhang, Hongnan and Ming Yu. 2019. "Photocatalytic Activity of TiO 2 Nanofibers : The Surface Crystalline Phase Matters."

20. Zhang, Qian, Yihe Zhang, Zilin Meng, Wangshu Tong, Xuelian Yu, and Qi An. 2017. "Constructing the Magnetic Bifunctional Graphene / Titania Nanosheet-Based Composite Photocatalysts for Enhanced Visible-Light Photodegradation of MB and Electrochemical ORR from Polluted Water." (September):1–11.

21. Zhao, Jiahuan, Yana Yang, Can Cui, Haihua Hu, Yichao Zhang, Juan Xu, Bingqing Lu, Lingbo Xu, Jiaqi Pan, and Weihua Tang. 2016. "TiO 2 Hollow Spheres as Light Scattering Centers in TiO 2 Photoanodes for Dye-Sensitized Solar Cells : The Effect of Sphere Diameter." Journal of Alloys and Compounds 663:211–16.

22. Zuorro, A., R. Lavecchia, M. M. Monaco, G. Iervolino, and V. Vaiano. 2019. “Photocatalytic Degradation of Azo Dye Reactive Violet 5 on Fe-Doped Titania Catalysts under Visible Light Irradiation.” Catalysts 9(8).
23. Hao, Meng Geng, Rong Min Dun, Yu Miao Su, and Wen Mu Li. 2020. “Highly Active Fe-N-Doped Porous Hollow Carbon Nanospheres as Oxygen Reduction Electrocatalysts in Both Acidic and Alkaline Media.” Nanoscale 12(28):15115–27.
24. Jiang, Xueliang, Chenjian Li, Song Liu, Fuqing Zhang, Feng You, and Chu Yao. 2017. “RSC Advances The Synthesis and Characterization of Ytterbium- Doped TiO 2 Hollow Spheres with Enhanced.” 24598–606.
25. Li, Hongliang. 2016. “Synthesis and Characterization of N-Doped Porous TiO 2 Hollow Spheres and Their Photocatalytic and Optical Properties.”
26. Merline. 2013. “Melamine Formaldehyde: Curing Studies and Reaction Mechanism.” Polymer Journal 45(4):413–19.
27. Microbeads, Glass. 2011. “Synthesis and Photocatalytic Activity of Fe-Doped TiO2 Supported on Hollow Synthesis and Photocatalytic Activity of Fe-Doped TiO 2 Supported on Hollow Glass Microbeads.” (November 2015):1–6.
28. Mishra, Gourav and Mausumi Mukhopadhyay. 2019. “TiO2 Decorated Functionalized Halloysite Nanotubes (TiO2@HNTs) and Photocatalytic PVC Membranes Synthesis, Characterization and Its Application in Water Treatment.” Scientific Reports 9(1):4345.
29. Sandoval, Sergio, Jian Yang, Jesus G. Alfaro, Alexander Liberman, Milan Makale, Casey E. Chiang, Ivan K. Schuller, Andrew C. Kummel, and William C. Trogler. 2012. “Europium-Doped TiO 2 Hollow Nanoshells: Two-Photon Imaging of Cell Binding.”
30. Wu, Youshen, Yan Li, Lei Qin, Feilong Yang, and Daocheng Wu. 2013. “Melamine – Formaldehyde Resin Polymer Colloidal.” 204–12.
31. Cai, Jiabai, Xueqing Wu, Fengying Zheng, Shunxing Li, Yaling Wu, Yanping Lin, Liting Lin, Biwen Liu, Qiaoying Chen, and Luxiu Lin. 2017. “Journal of Colloid and Interface Science Influence of TiO 2 Hollow Sphere Size on Its Photo-Reduction Activity for Toxic Cr (VI) Removal.” Journal of Colloid And Interface Science 490:37–45.
32. Islam, Syed Z., Suraj Nagpure, Doo Young Kim, and Stephen E. Rankin. 2017. “Synthesis and Catalytic

Applications of Non-Metal Doped Mesoporous Titania.” Inorganics 5(1):1–42.

33. Liu, Beibei, Jin Wang, Junhua Li, Kaili Fan, Dan Zhao, Guiyu Liu, and Chunming Yang. 2019. “Journal of Physics and Chemistry of Solids N-Doped Carbon Coated TiO 2 Hollow Spheres as Ultralong-Cycle-Life Na-Ion Battery Anodes.” Journal of Physical and Chemistry of Solids 134(June):214–24.
34. Liu, Ruiping, Feng Ren, Weiming Su, Peng He, Chao Shen, Lei Zhang, and Chang-an Wang. 2015. “Synthesis of TiO2 Hollow Spheres with Tunable Pore Structure and Enhanced Photocatalytic Activity Synthesis of TiO 2 Hollow Spheres with Tunable Pore Structure and Enhanced Photocatalytic Activity.” Ceramics International 41(10):14615–20.
35. Qiao, Min, Qiang Chen, and Shishan Wu. 2010. “Novel Sol – Gel Synthesis of N-Doped TiO2 Hollow Spheres with High Photocatalytic Activity Under Visible Light Novel Sol – Gel Synthesis of N-Doped TiO 2 Hollow Spheres with High Photocatalytic Activity under Visible Light.” (May 2014).
36. Seif, Amirmohammad, Alireza Nikfarjam, and Hassan Haj. 2019. “Sensors and Actuators B : Chemical UV Enhanced Ammonia Gas Sensing Properties of PANI / TiO 2 Core-Shell Nanofibers.” Sensors & Actuators: B. Chemical 298(December 2018):126906.
37. Wan, Hengcheng, Weitang Yao, Wenkun Zhu, Yi Tang, Huilin Ge, Xiaozhong Shi, and Tao Duan. 2018. “Fe-N Co-Doped SiO2@TiO2 Yolk-Shell Hollow Nanospheres with Enhanced Visible Light Photocatalytic Degradation.” Applied Surface Science 444:355–63.
38. Wang, Qianqian, Shengli Zhu, Yanqin Liang, Zhenduo Cui, Xianjin Yang, Chunyong Liang, and Akihisa Inoue. 2017. “Synthesis of Br-Doped TiO2 Hollow Spheres with Enhanced Photocatalytic Activity.” Journal of Nanoparticle Research 19(2).
39. Zarnaghash, Narges, Ramin Rezaei, Payam Hayati, and Mohammad Mahdi. 2019. “Materials Science & Engineering C Selective Ultrasonic Assisted Synthesis of Iron Oxide Mesoporous Structures Based on Sulfonated Melamine Formaldehyde and Survey of Nanorod / Sphere , Sphere and Core / Shell on Their Catalysts Properties for the Biginell.” Materials Science & Engineering C 104(July):109975.
40. Zhang, Jinxi, Baoshan Li, and Wangliang Yang. 2014. “Synthesis and Photocatalytic Performance of Novel Hierarchical Hollow Silica Sphere Supported TiO 2 Nanoparticles.” Materials Letters 117:252–55.
41. Zhuang, Jiandong, Hu Zhou, and Qian Liu. 2013. “Facile Solvothermal Method to Synthesis Eu Doped TiO 2 Hollow Microspheres with Enhanced Photoluminescence.” 638:2198–2202.

42. Alosfur, Firas K. Mohamad and Noor J. Ridha. 2018. “One-Step Formation of TiO 2 Hollow Spheres via a Facile Microwave-Assisted Process for Photocatalytic Activity.”

43. Kumaravel, Vignesh, Stephen Rhatigan, Snehamol Mathew, John Bartlett, Michael Nolan, Steven J. Hinder, Preetam K. Sharma, Anukriti Singh, J. Anthony Byrne, John Harrison, and Suresh C. Pillai. 2019. “Indium-Doped TiO 2 Photocatalysts with High-Temperature Anatase Stability.” The Journal of Physical Chemistry C 123:21083–96.

44. Liu, Hui, Hongliang Li, Zhaolong Ding, and Aiping Fu. 2012. “Preparation of Porous Hollow SiO 2 Spheres ¨ Ber Process Using MF Microspheres by a Modified Sto as Templates.” 273–85.

45. Shang, Shuqin, Xiuling Jiao, and Dairong Chen. 2012. “Template-Free Fabrication of TiO 2 Hollow Spheres and Their Photocatalytic Properties.”

46. Microbeads, Glass. 2011. “Synthesis and Photocatalytic Activity of Fe-Doped TiO2 Supported on Hollow Synthesis and Photocatalytic Activity of Fe-Doped TiO 2 Supported on Hollow Glass Microbeads.” (November 2015):1–6.

47. Anwar, Devi Indah and Dikdik Mulyadi. 2015. “Synthesis of Fe-TiO 2 Composite as a Photocatalyst for Degradation of Methylene Blue.” Procedia Chemistry 17:49–54.

48. Jiang, Xueliang, Chenjian Li, Song Liu, Fuqing Zhang, Feng You, and Chu Yao. 2017. “RSC Advances The Synthesis and Characterization of Ytterbium- Doped TiO 2 Hollow Spheres with Enhanced.” 24598–606.

49. Kamble, Ravi, Smita Mahajan, Vijaya Puri, Harish Shinde, and Kalayanrao Garadkar. 2018. “Material Science Research India Visible Light-Driven High Photocatalytic Activity of Cu-Doped TiO 2 Nanoparticles Synthesized by Hydrothermal Method.” 15(3).

50. Li, Hongliang. 2016. “Synthesis and Characterization of N-Doped Porous TiO 2 Hollow Spheres and Their Photocatalytic and Optical Properties.”

51. Li, Jing and Hua Chun Zeng. 2007. “Hollowing Sn-Doped TiO 2 Nanospheres via Ostwald Ripening.” (16):495–503.

52. Lu, Jing, Yong Wang, Jianfeng Huang, Jie Fei, Liyun Cao, and Cuiyan Li. 2017. “Dyes and Pigments In Situ Synthesis of Mesoporous C-Doped TiO 2 Single Crystal with Oxygen Vacancy and Its Enhanced Sunlight Photocatalytic Properties.” Dyes and Pigments 144:203–11.

53. Mital, Gupta Shipra and Tripathi Manoj. 2011. "A Review of TiO 2 Nanoparticles." 56(16):1639–57.

54. Peng, Bo, Xianwei Meng, Fangqiong Tang, Xiangling Ren, Dong Chen, and Jun Ren. 2009. "General Synthesis and Optical Properties of Monodisperse Multifunctional Metal-Ion-Doped TiO2 Hollow Particles." Journal of Physical Chemistry C 113(47):20240–45.

55. Peng, Hong, Jie Cui, Hongju Zhan, and Xu Zhang. 2015. "Improved Photodegradation and Detoxification of 2 , 4 , 6-Trichlorophenol by Lanthanum Doped Magnetic TiO 2." CHEMICAL ENGINEERING JOURNAL 264:316–21.

56. Qiao, Min, Qiang Chen, and Shishan Wu. 2010. "Novel Sol – Gel Synthesis of N-Doped TiO2 Hollow Spheres with High Photocatalytic Activity Under Visible Light Novel Sol – Gel Synthesis of N-Doped TiO 2 Hollow Spheres with High Photocatalytic Activity under Visible Light." (May 2014).

57. Saravanan, R., Devaraj Manoj, Jiaqian Qin, Mu Naushad, F. Gracia, Adam F. Lee, Mohammad Mansoob Khan, and M. A. Gracia-Pinilla. 2018. "Mechanothermal Synthesis of Ag/TiO2 for Photocatalytic Methyl Orange Degradation and Hydrogen Production." Process Safety and Environmental Protection 120:339–47.

58. Shi, Jiangbo, Guiqiu Chen, Guangming Zeng, Anwei Chen, Kai He, Zhenzhen Huang, Liang Hu, Jingwen Zeng, Jing Wu, and Weiwei Liu. 2018. "Hydrothermal Synthesis of Graphene Wrapped Fe-Doped TiO2 Nanospheres with High Photocatalysis Performance." Ceramics International 44(7):7473–80.

59. Shi, Jiayuan, Jiangyao Chen, Guiying Li, Taicheng An, and Hiromi Yamashita. 2017. "Fabrication of Au / TiO 2 Nanowires @ Carbon Fiber Paper Ternary Composite for Visible-Light Photocatalytic Degradation of Gaseous Styrene." Catalysis Today 281:621–29.

60. Shogh, Shiva, Raheleh Mohammadpour, Azam Iraji, and Nima Taghavinia. 2015. "Improved Photovoltaic Performance of Nanostructured Solar Cells by Neodymium-Doped TiO 2 Photoelectrode." Materials Letters 159:273–75.

61. Singh, Kamaljeet, S. Harish, J. Archana, M. Navaneethan, and M. Shimomura. 2019. "Applied Surface Science Investigation of Gd-Doped Mesoporous TiO 2 Spheres for Environmental Remediation and Energy Applications." Applied Surface Science 489(May):883–92.

62. Song, Hongbing, Zong Liu, Yongjie Wang, Na Zhang, Xiaofei Qu, Kai Guo, and Meng Xiao. 2019. "ScienceDirect Template-Free Synthesis of Hollow TiO 2 Nanospheres Supported Pt for Selective Photocatalytic Oxidation of Benzyl Alcohol to Benzaldehyde." Green Energy and Environment

4(3):278–86.

63. Wang, Qi, Zenan Qin, Jie Chen, Baosheng Ren, Qifeng Chen, Yanchuan Guo, and Xiaofeng Cao. 2016. “Applied Surface Science Green Synthesis of Nickel Species in Situ Modified Hollow Microsphere TiO 2 with Enhanced Photocatalytic Activity.” Applied Surface Science 364:1–8.

64. Wang, Qianqian, Shengli Zhu, Yanqin Liang, Zhenduo Cui, Xianjin Yang, Chunyong Liang, and Akihisa Inoue. 2017. “Synthesis of Br-Doped TiO2 Hollow Spheres with Enhanced Photocatalytic Activity.” Journal of Nanoparticle Research 19(2).

65. Xie, Wei, Rui Li, and Qingyu Xu. 2018. “Enhanced Photocatalytic Activity of Se-Doped TiO 2 under Visible Light Irradiation.” Scientific Reports 1–10.

66. Yin, Jian B. and Xiao P. Zhao. 2006. “Enhanced Electrorheological Activity of Mesoporous Cr-Doped TiO 2 from Activated Pore Wall and High Surface Area.” (86):12916–25.

67. Zhuang, Jiandong, Hu Zhou, and Qian Liu. 2013. “Facile Solvothermal Method to Synthesis Eu Doped TiO 2 Hollow Microspheres with Enhanced Photoluminescence.” 638:2198–2202.

APPENDIX

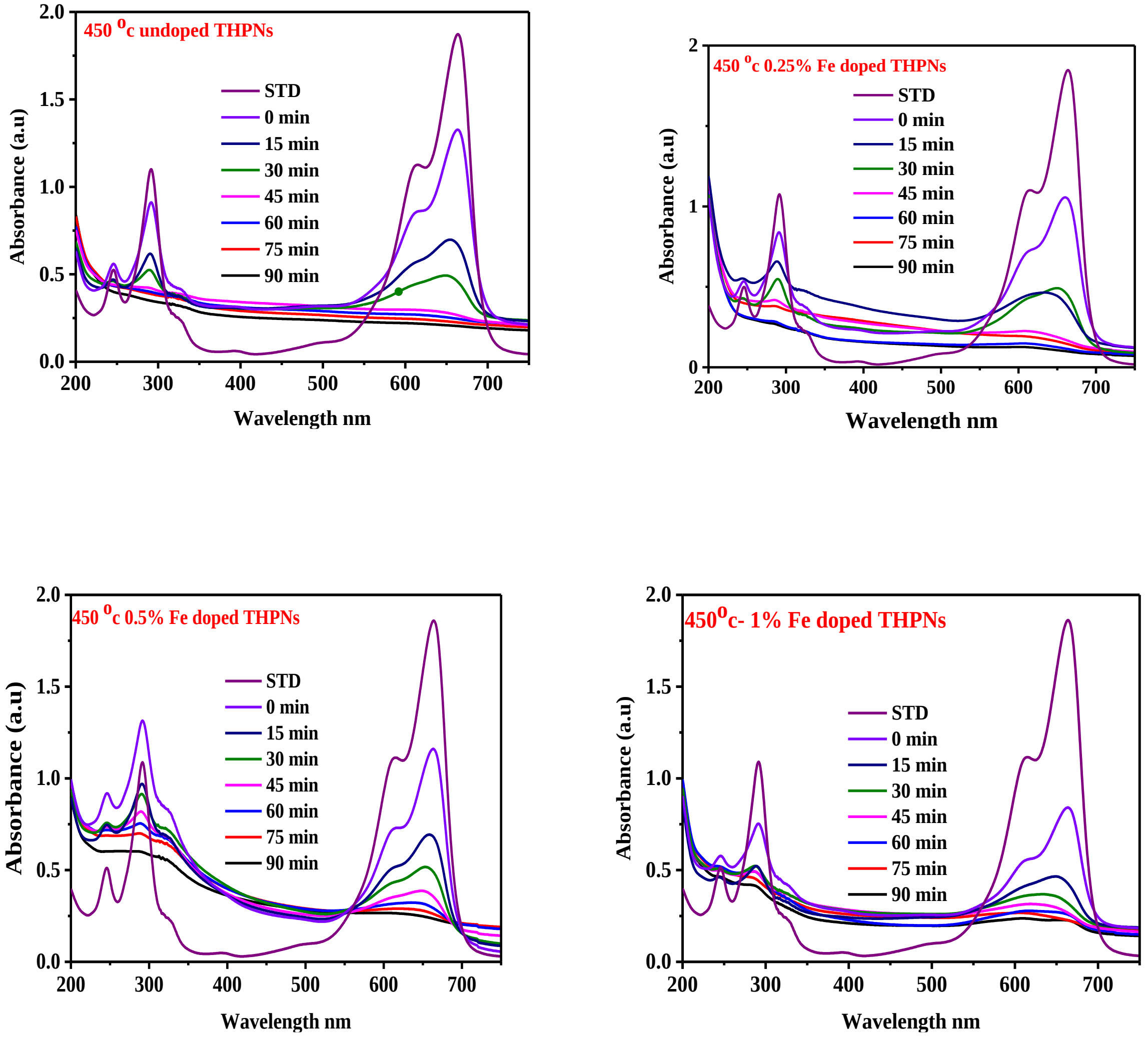

Appendix 1- Degradation of MB using Fe doped and undoped THPNS at 450 ^{o}C in 15 minute intervals.

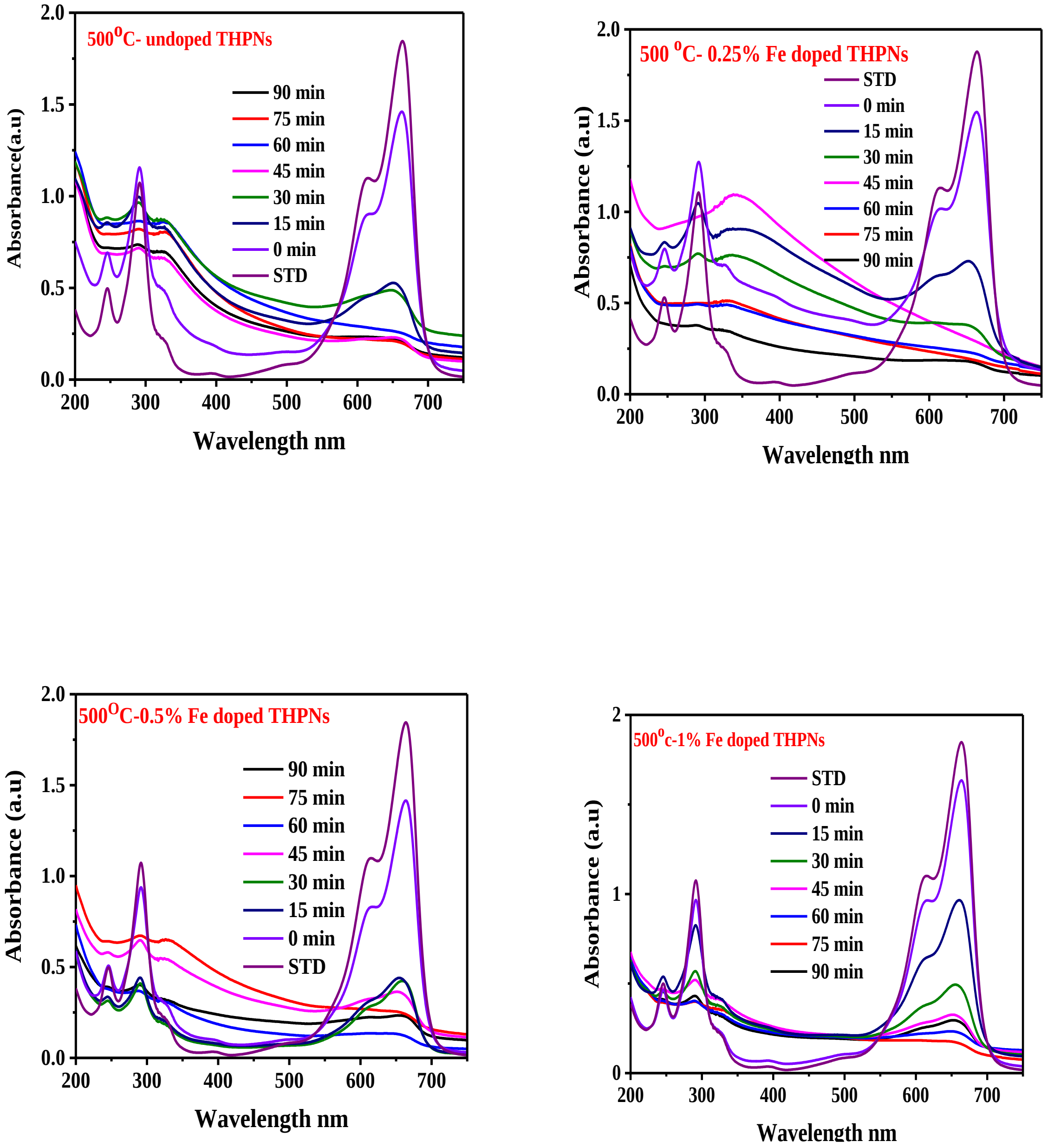

Appendix 2 Degradation of MB using Fe doped undoped THPNS at 500°C in 15-minute interval.

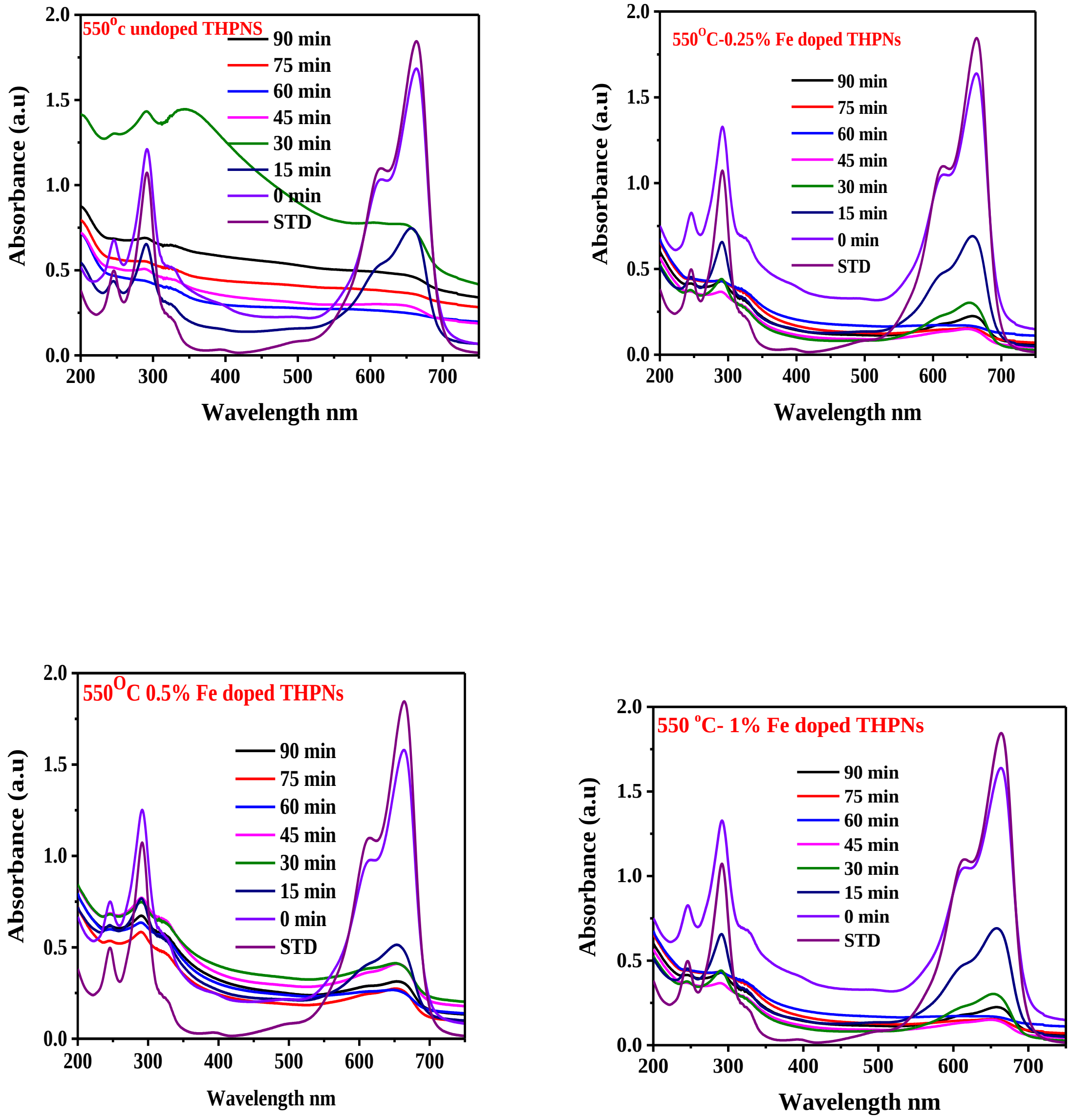

Appendix 3-Degradation of MB using Fe doped and undoped THPNS at 550°C in 15minute interval.

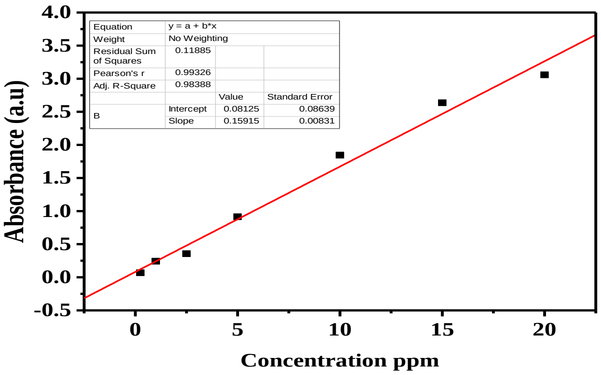

Equation	y = a + b*x		
Weight	No Weighting		
Residual Sum of Squares	0.11885		
Pearson's r	0.99326		
Adj. R-Square	0.98388		
		Value	Standard Error
B	Intercept	0.08125	0.08639
	Slope	0.15915	0.00831

Appendix 4 calibration curve of dye in different concentrations.

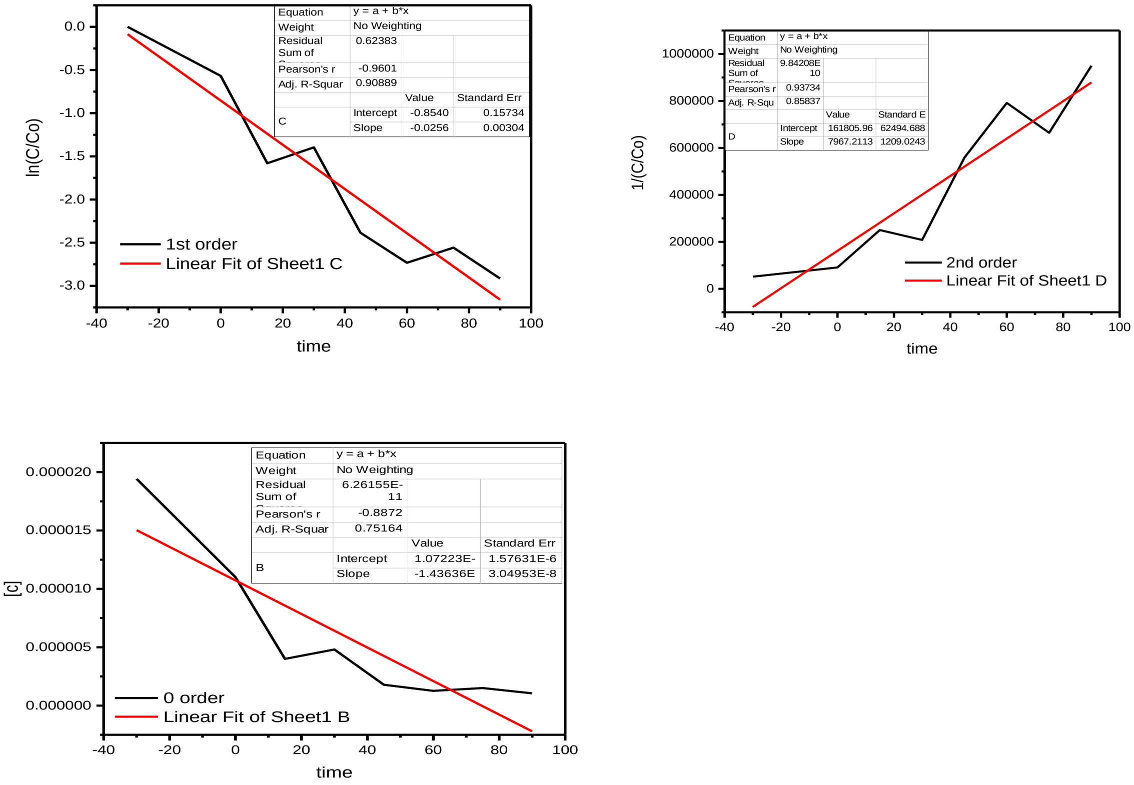

Equation	y = a + b*x		
Weight	No Weighting		
Residual Sum of	0.62383		
Pearson's r	-0.9601		
Adj. R-Squar	0.90889		
		Value	Standard Err
C	Intercept	-0.8540	0.15734
	Slope	-0.0256	0.00304

Equation	y = a + b*x		
Weight	No Weighting		
Residual Sum of	9.84208E 10		
Pearson's r	0.93734		
Adj. R-Squ	0.85837		
		Value	Standard E
D	Intercept	161805.96	62494.688
	Slope	7967.2113	1209.0243

Equation	y = a + b*x		
Weight	No Weighting		
Residual Sum of	6.26155E-11		
Pearson's r	-0.8872		
Adj. R-Squar	0.75164		
		Value	Standard Err
B	Intercept	1.07223E-	1.57631E-6
	Slope	-1.43636E	3.04953E-8

Appendix 5- 0, 1st, and 2nd order reaction to indicate R^2 value.